JM PAPERS

An improved Baldwin–Lomax algebraic wall model for high-speed canonical turbulent boundary layers using established scalings

Xianliang Chen[1], **Jianping Gan**[1,2] **and Lin Fu**[1,3,4],†

[1]Department of Mathematics and Center for Ocean Research in Hong Kong and Macau (CORE), The Hong Kong University of Science and Technology, Clear Water Bay, Kowloon, Hong Kong, PR China

[2]Department of Ocean Science, The Hong Kong University of Science and Technology, Clear Water Bay, Kowloon, Hong Kong, PR China

[3]Department of Mechanical and Aerospace Engineering, The Hong Kong University of Science and Technology, Clear Water Bay, Kowloon, Hong Kong, PR China

[4]HKUST Shenzhen-Hong Kong Collaborative Innovation Research Institute, Futian, Shenzhen 518045, PR China

In this work, we employ well-established relations for compressible turbulent mean flows, including the velocity transformation and algebraic temperature–velocity (TV) relation, to systematically improve the algebraic Baldwin–Lomax (BL) wall model for high-speed zero-pressure-gradient air boundary layers. Any new functions or coefficients fitted by ourselves are avoided. Twelve published direct numerical simulation (DNS) datasets are employed for *a priori* inspiration and *a posteriori* examination, with Mach numbers up to 14 under adiabatic, cold and heated walls. The baseline BL model is the widely used one with semilocal scalings. Three targeted modifications are made. First, we employ a total-stress-based transformation (Griffin *et al.*, *Proc. Natl Acad. Sci. USA*, vol. 118, issue 34, 2021, e2111144118) to the inner-layer eddy viscosity for improved scaling up to the logarithmic region. Second, we utilize the van Driest transformation in the outer layer based on the compressible defect velocity scaling. Third, considering the difficulty in modelling the rapidly varying and singular turbulent Prandtl number near the temperature peak in cold-wall cases, we design a two-layer strategy and use the TV relation to formulate the inner-layer temperature. Numerical results prove that the modifications take effect as designed. The prediction accuracy for mean streamwise velocity is notably improved for diabatic cases, especially in the logarithmic region. Moreover, a significant improvement

† Email address for correspondence: linfu@ust.hk

in mean temperature is realized for both adiabatic and diabatic cases. The mean relative errors of temperature to DNS for all cases are down to 0.4 % in the logarithmic wall-normal coordinate and 3.4 % in the outer coordinate, around one-third of those in the baseline model.

Key words: turbulent boundary layers, turbulence theory, turbulence modelling

1. Introduction

In high-speed flows, turbulent boundary layers are known to severely affect the surface drag and heat transfer, so accurate predictive models are strongly desired for reliable vehicle design and flow control (Bradshaw 1977). Among various simulation strategies, the Reynolds-averaged Navier–Stokes (RANS) models are long established yet still prevailing, especially for engineering problems, owing to their simplicity, efficiency and robustness (Wilcox 2006). Compared with the incompressible counterpart, however, compressible RANS models have weaker theoretical foundations, and suffer from the complications brought about by intrinsic compressibility, heat transfer, shocks, high-enthalpy effects and other factors (Gatski & Bonnet 2013; Cheng *et al.* 2024).

The RANS models are usually divided into four categories by the number of additional equations introduced: the algebraic (zero-equation), one-equation, two-equation and stress-transport models. The algebraic models are the simplest ones, which directly model the eddy viscosity μ_t (and eddy diffusivity κ_t) using theoretical/empirical algebraic relations. Two standout models are the Cebeci–Smith (CS) model (Cebeci & Smith 1974) and the Baldwin–Lomax (BL) model (Baldwin & Lomax 1978), both of which formulate μ_t into a two-layer structure. The inner layer part is based on the mixing length model with a viscous damping correction devised by van Driest (1956). The outer portion is built on the defect layer scaling by Clauser (1956) and the intermittent function by Klebanoff (1955). In incompressible applications, the algebraic models can faithfully reproduce mean velocity profiles and skin friction for attached boundary layers, though they become unreliable when subject to strong pressure gradient and separation (Wilcox 2006). Furthermore, the CS and BL models can attain comparable accuracy levels. The latter is more commonly considered for complex flows since it avoids directly using the boundary layer thickness. When extended to compressible flows, no special compressibility correction was considered in early investigations, observing the insensitivity of classical mixing length to the Mach number *Ma* (Maise & McDonald 1968; Baldwin & Lomax 1978). To close the problem, κ_t in the energy equation is related to μ_t through a prescribed turbulent Prandtl number Pr_t. The resulting compressible models can reproduce well the mean flows in high-speed adiabatic flows with minor pressure gradients, but they deteriorate under diabatic walls (with surface heat transfer; (Maise & McDonald 1968; Shang, Hankey & Dwoyer 1973; York & Knight 1985)). As one improvement, the wall viscous unit for the inner layer scaling can be replaced by the semilocal one (though not in this terminology originally) based upon local density and viscosity (Gupta *et al.* 1990; Cheatwood & Thompson 1993). Dilley & McClinton (2001) showed that this modification in BL largely improved the mean flows in hypersonic cold-wall cases, and the predicted surface friction and heat flux agreed well with experiments. Further improvements for complex three-dimensional boundary layers were contributed by, for example, Degani & Schiff (1983) and Panaras (1997), among others. Consequently, the BL models are extensively adopted in high-speed applications

and numerous commercial solvers (Cheatwood & Thompson 1993; Srinivasan, Bittner & Bobskill 1993; Rumsey, Biedron & Thomas 1997; Townend *et al.* 1999; Candler *et al.* 2015).

On the other hand, recently accumulated direct numerical simulation (DNS) data for high-speed canonical flows provides a chance to reassess the behaviour of the BL model. As analysed by Hendrickson *et al.* (2023), and as will be shown below, even for zero-pressure-gradient (ZPG) flat-plate boundary layers, there are clear disparities in mean profiles between BL and DNS under diabatic conditions, especially for the temperature. Also, there is room for improvement in adiabatic flows. Therefore, the objective of this work is to improve the velocity and temperature prediction by the BL model for canonical supersonic/hypersonic boundary layers, based on recently advanced knowledge of mean flow properties.

The established relations of mean velocity and temperature in compressible wall-bounded turbulence are briefly reviewed, to set the grounds for later discussions. First, the hypothesis of Morkovin (1962) earns wide support, which states that at moderate free stream Mach numbers ($Ma_\infty \lesssim 5$), the dilatation effect is small, so any differences from incompressible turbulence can be accounted for by variations of mean properties (Coleman, Kim & Moser 1995; Pirozzoli, Grasso & Gatski 2004; Duan, Beekman & Martín 2010; Lagha *et al.* 2011). As a result, velocity transformation can be built using only mean flow variables, expecting that the transformed streamwise velocity reproduces the incompressible law of the wall and outer-layer scalings. More attention has been paid to the former, i.e. the compressible law of the wall. Pioneering work is the transformation by van Driest (1951) (denoted as VD hereinafter) built upon the mixing length assumption. This widely used transformation performs well for high-speed adiabatic flows, but deteriorates in diabatic conditions. Trettel & Larsson (2016) designed a transformation based on viscous stress and semilocal units (denoted as TL), which is particularly accurate for pipe and channel flows, but can also become less accurate in diabatic boundary layers (logarithmic region). Recently, Griffin, Fu & Moin (2021) proposed a total-stress-based transformation (denoted as GFM), combining the advantages of the near-wall relation by TL and a modified version of the equilibrium arguments of Zhang *et al.* (2012). The GFM transformation performs remarkably well in a wide range of air flows, particularly diabatic flows, hence successfully collapsing the channel, pipe and boundary layer cases within and below the logarithmic region. Very recently, Hasan *et al.* (2023*b*) proposed a transformation (termed HLPP) by introducing a correction to the TL transformation to interpret intrinsic compressibility effects (hence questioning the validity of Morkovin's hypothesis), so the logarithmic scaling in diabatic flows can be reasonably formulated. Besides, the non-air-like and supercritical flow cases can be accounted for, which can be a challenge for the GFM transformation (Bai, Griffin & Fu 2022). On the other hand, fewer transformations are available for the outer-layer velocity, presumably due to the greater reliance on flow configurations. Maise & McDonald (1968) demonstrated that a compressible law of the wake was attainable for adiabatic boundary layers (Ma_∞ from 1.5 to 5) using the VD transformation. Duan, Beekman & Martín (2011) (and also Guarini *et al.* (2000), Pirozzoli *et al.* (2004) and Wenzel *et al.* (2018)) suggest that the VD-transformed velocities collapse in the outer layer for adiabatic boundary layers with Ma_∞ from 0 to 12, provided comparable Re_{δ_2} (defined later). Pirozzoli & Bernardini (2011) also noted that for supersonic adiabatic boundary layers, the VD-transformed defect velocity matched the incompressible counterpart well.

In terms of temperature, the classical Crocco–Busemann relation (e.g. White 2006) shows that, after assuming unity Prandtl numbers (*Pr*), the mean temperature is almost

a quadratic function of the mean streamwise velocity. A less restrictive relation was proposed by Walz (1969) to incorporate non-unity *Pr* effects by introducing the recovery temperature. Although this relation holds in high-speed adiabatic flows, the accuracy degrades severely in case of significant surface heat transfer. A crucial modification was contributed by Duan & Martín (2011), who introduced a semiempirical quadratic function of the velocity. The resulting quadratic temperature–velocity (TV) relation was shown to be highly accurate for a wide range of boundary layer, channel and pipe flows (Zhang, Duan & Choudhari 2018; Modesti & Pirozzoli 2019; Fu *et al.* 2021; Griffin, Fu & Moin 2023), even with high-enthalpy effects (using enthalpy instead; Passiatore *et al.* 2022). Subsequently, Zhang *et al.* (2014) recast the above relation in terms of a generalized Reynolds analogy, where the Reynolds analogy factor is present for further physical interpretations of the closure constant.

The success of these mean flow relations makes it possible to recover the mean velocity and temperature by solving an inverse problem, which helps improve turbulence modelling. Pioneering work is the generalized velocity derived by van Driest (1951) through combining the VD transformation and the quadratic TV relation throughout the boundary layer. This framework enables efficient computation of the mean profiles and skin friction (Huang, Bradshaw & Coakley 1993; Kumar & Larsson 2022). Owing to the continuously increased accuracy of these mean flow relations, more and more attention has been paid to the modelling aspect in recent years. For channel and pipe flows, the combination of the velocity transformation and TV relation leads to ordinary differential equations (ODEs) for the mean flow, which achieves a relatively high accuracy (Chen *et al.* 2023*a*; Song, Zhang & Xia 2023). For ZPG boundary layers, Hasan *et al.* (2023*a*) supplemented a *Re*-dependent function for Coles' wake parameter (Coles 1956). The ODE set for the inverse problem is thus formulated, and the results are in close agreement with DNS. In a more general set-up, Hendrickson, Subbareddy & Candler (2022) and Hendrickson *et al.* (2023) used velocity transformations to improve the inner-layer scaling of the BL model, also for ZPG boundary layers. Although the mean profile prediction is improved for the two cases displayed, there are still noticeable deviations in temperature from DNS for cold-wall cases. More encouragingly, the established relations can help improve the wall-modelled large-eddy simulations (WMLES). In a very recent work, Griffin *et al.* (2023) proposed a near-wall model using the GFM transformation and the TV relation, with the outer boundary conditions provided by large-eddy simulations (LES). This model was shown to be significantly more accurate than the classical ODE wall model for a wide range of canonical cases examined. Hendrickson *et al.* (2023) made similar explorations, while the temperature prediction was less accurate for cold-wall boundary layers when velocity transformations alone were taken into account.

As aforementioned, we aim to improve the compressible BL model for canonical boundary layers using the established relations for mean velocity and temperature. To make the improvement clean and solid, we strictly adhere to the following three principles.

(i) First, the BL model for incompressible flows is not altered. The compressible version is modified to achieve the same accuracy level as the incompressible one.

(ii) Second, only well-established relations are used, which have been widely verified. We avoid introducing any new functions or coefficients fitted by ourselves.

(iii) Last, the modification is made as simple as feasible.

For *a priori* inspiration and *a posteriori* examination, wide published DNS databases for ZPG boundary layers are employed containing 12 cases from different sources, with Ma_∞
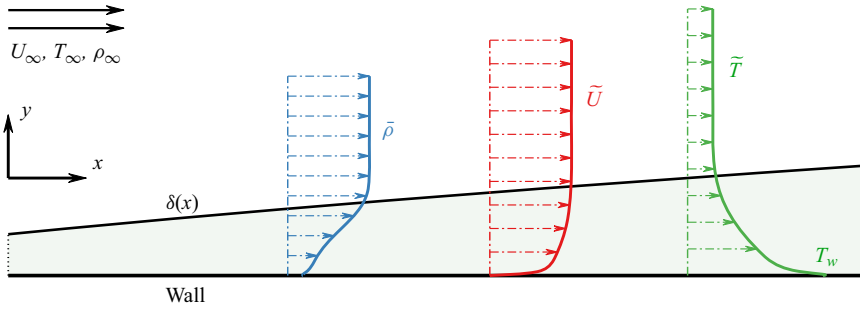
Figure 1. Schematic of the compressible flat-plate ZPG boundary layers.

ranging from 2 to 14 under adiabatic, cold and heated wall conditions. Of particular focus are the cold-wall cases, which are ubiquitous and even unavoidable in practical hypersonic applications. The remaining parts are organized as follows. Section 2 describes the governing equations, DNS database and the baseline BL model. Section 3 presents how established relations are implemented in the wall model, and provides *a priori* examination using the DNS data. The resulting modified BL model is examined in § 4 for all the cases, and the work is summarized in § 5. Although only ZPG boundary layers are considered, we believe that the present framework is promising. The applications, limitations and future steps are discussed in § 5.1.

2. Problem formulations and datasets

2.1. *Governing equations and DNS datasets*

The ZPG turbulent boundary layers are considered, as illustrated in figure 1. Assuming a calorically perfect gas, the zero-equation RANS equations are written as

$$\frac{\partial \bar{\rho}}{\partial t} + \nabla \cdot (\bar{\rho}\tilde{u}) = 0, \qquad (2.1a)$$

$$\bar{\rho}\left(\frac{\partial \tilde{u}}{\partial t} + \tilde{u} \cdot \nabla \tilde{u}\right) = -\nabla \bar{p} + \nabla \cdot \left[(\tilde{\mu} + \mu_t)\left(\nabla \tilde{u} + \nabla \tilde{u}^{\mathrm{T}}\right)\right] - \frac{2}{3}\nabla\left[(\tilde{\mu} + \mu_t)\nabla \cdot \tilde{u}\right], \qquad (2.1b)$$

$$\bar{\rho}c_p\left(\frac{\partial \tilde{T}}{\partial t} + \tilde{u} \cdot \nabla \tilde{T}\right) - \left(\frac{\partial \bar{p}}{\partial t} + \tilde{u} \cdot \nabla \bar{p}\right)$$

$$= (\tilde{\mu} + \mu_t)\left[\nabla \tilde{u} : \left(\nabla \tilde{u} + \nabla \tilde{u}^{\mathrm{T}}\right) - \frac{2}{3}\left(\nabla \cdot \tilde{u}\right)^2\right] + \nabla \cdot \left[(\tilde{\kappa} + \kappa_t)\nabla \tilde{T}\right], \qquad (2.1c)$$

where ρ, u, T and $p = \rho RT$ are the fluid's density, velocity, temperature and pressure; R and c_p are the gas constant and isobaric specific heat; μ and κ are molecular viscosity and thermal conductivity. The Reynolds and Favre averages are denoted as $\bar{\phi}$ and $\tilde{\phi}$ (fluctuations as ϕ' and ϕ''), respectively. The quantities μ_t and κ_t model the Reynolds stress $-\bar{\rho}\widetilde{u''u''}$ and turbulent heat flux $-\bar{\rho}c_p\widetilde{u''T''}$, whose formulations are described in § 2.3. The wall is set no-slip and isothermal or adiabatic. The variables in wall viscous units are expressed with a superscript +, as $x^+ = x/\delta_v$, $\bar{\rho}^+ = \bar{\rho}/\rho_w$, $\tilde{u}^+ = \tilde{u}/u_\tau$ and $\tilde{\mu}^+ = \tilde{\mu}/\mu_w$, where w represents the wall variables, $\delta_v = \mu_w/(\rho_w u_\tau)$ is the viscous length unit, $u_\tau = (\tau_w/\rho_w)^{1/2}$ is the friction velocity, τ_w is the wall shear. Correspondingly, the friction

No.	Source	Notation	Ma_∞	T_w/T_r	Re_θ	Re_τ
0-(1–5)	SO	M0R14–R41	0	—	1420–4060	492–1272
1-(1–4)	PB	M2Tw10R13–R39	2	1	2080–6040	447–1113
2-(1–2)	PB	M3Tw10R14–R18	3	1	3310–4340	403–502
3-(1–2)	PB	M4Tw10R17–R21	4	1	4710–5910	398–505
4	ZDC	M2p5Tw10R17	2.50	1	2835	510
5	VBL	M2Tw05R13	2.28	0.5	1250	512
6-(1–2)	VBL	M5Tw08R13–R23	5	0.8	3770–6980	389–685
7	ZDC	M6Tw025R11	5.84	0.25	2121	450
8	ZDC	M6Tw076R17	5.86	0.76	9455	453
9	ZDC	M8Tw048R20	7.87	0.48	9714	480
10	ZDC	M14Tw018R24	13.64	0.18	14 408	646
11	VBL	M2Tw19R3	2.28	1.9	870	100
12	VBL	M5Tw19R7	5	1.9	3900	176

Table 1. Parameters for the DNS datasets, where T_r is the recovery temperature ($T_w = T_r$ for adiabatic cases). The cases with multiple streamwise locations are labelled in the brackets of the case numbers. The abbreviations for data sources are used hereinafter, as SO for Schlatter & Örlü (2010), PB for Pirozzoli & Bernardini (2011, 2013), ZDC for Zhang *et al.* (2018) and VBL for Volpiani *et al.* (2018, 2020). The notation expresses Ma_∞, T_w/T_r and Re_{δ_2} (divided by 100).

Reynolds number is $Re_\tau = \delta_{99}/\delta_v$ with δ_{99} the nominal thickness based on streamwise velocity. Furthermore, semilocal units are adopted, with a superscript $*$ as $u_\tau^* = (\tau_w/\bar{\rho})^{1/2}$, $\delta_v^* = \tilde{\mu}/(\bar{\rho}u_\tau^*)$, so $y^* = y/\delta_v^*$. Most recent transformations are based on y^*, so y^* as the inner scaling can be used to classify different layers, in analogy to y^+ in incompressible flows. Besides, two commonly used Reynolds numbers are $Re_\theta = \rho_\infty U_\infty \theta/\mu_\infty$ and $Re_{\delta_2} = \rho_\infty U_\infty \theta/\mu_w$ (Fernholz & Finley 1980), where θ is the momentum thickness and ∞ denotes free stream variables.

To comprehensively examine the modified BL model, wide elaborated DNS databases are employed for ZPG boundary layers from different sources, with Ma_∞ from 2 to 14 under adiabatic, cold and heated walls. The published data are from Pirozzoli & Bernardini (2011, 2013), Zhang *et al.* (2018) and Volpiani, Bernardini & Larsson (2018, 2020), as summarized in table 1. Though $Ma_\infty = 14$ is reached, the high-enthalpy effects (e.g. Chen *et al.* 2022*b*) are not considered following the reference set-up. Besides, the incompressible data from Schlatter & Örlü (2010) are included, as a reference for the incompressible BL model. The viscous parameters in each case are computed according to the references. The viscosity is from Sutherland's law, the power law or the formula for N_2 (the working fluid in case ZDC-M8Tw048R20). Constant $Pr = c_p\mu/\kappa$ are adopted for the thermal conductivity.

Notably, (2.1) is expressed using the Favre-averaged variables (except for $\bar{\rho}$) to form a closed system (Gatski & Bonnet 2013). The difference between the Reynolds- and Favre-averaged results cannot be accounted for using the algebraic RANS models, so we simply use the Favre averages throughout for consistency of notation, though the DNS data mostly adopt the Reynolds averages. This simplification will not affect the main conclusions of this work because even for the M14Tw018R24 case of the highest Ma, there are only slight differences between the DNS statistics from these two averages (Zhang *et al.* 2018).

2.2. *Solution of boundary layer equations*

Based on the hypersonic interaction parameter (White 2006), the effects of shock-boundary-layer interaction at the leading edge are evaluated to be minor on the downstream locations for the cases in table 1. Therefore, the boundary layer equations can be used for efficient computation of the mean flow, in the absence of impinging shock and separation. From (2.1), the boundary layer equations are written as (e.g. White 2006)

$$
\left.
\begin{aligned}
\frac{\partial(\bar{\rho}\tilde{U})}{\partial x} + \frac{\partial(\bar{\rho}\tilde{V})}{\partial y} &= 0, \\
\bar{\rho}\left(\tilde{U}\frac{\partial\tilde{U}}{\partial x} + \tilde{V}\frac{\partial\tilde{U}}{\partial y}\right) &= -\frac{\mathrm{d}P_e}{\mathrm{d}x} + \frac{\partial}{\partial y}\left[(\tilde{\mu} + \mu_t)\frac{\partial\tilde{U}}{\partial y}\right], \\
\bar{\rho}c_p\left(\tilde{U}\frac{\partial\tilde{T}}{\partial x} + \tilde{V}\frac{\partial\tilde{T}}{\partial y}\right) &= \tilde{U}\frac{\mathrm{d}P_e}{\mathrm{d}x} + (\tilde{\mu} + \mu_t)\left(\frac{\partial\tilde{U}}{\partial y}\right)^2 + \frac{\partial}{\partial y}\left[(\tilde{\kappa} + \kappa_t)\frac{\partial\tilde{T}}{\partial y}\right],
\end{aligned}
\right\} \quad (2.2)
$$

where $\tilde{U}$ and $\tilde{V}$ are the streamwise (x) and wall-normal (y) velocities. The pressure is assumed invariant along the y-direction (P_e), so $\bar{\rho} = \rho_e T_e/\tilde{T}$ is satisfied, where e denotes values at the boundary layer edge. More general formulations accounting for geometrical curvature, far-field shock and cross-flow can be found in Degani & Schiff (1983) and Gupta *et al.* (1990).

Due to the complex formulation of μ_t and κ_t (§ 2.3), the boundary layer profiles are not self-similar, even with ZPG. To solve the non-self-similar flow, the Mangler–Levy–Lees transformation can be used to remove the singularity at the leading edge $x = 0$ (Probstein & Elliott 1956). The transformed coordinate (ξ, η) is defined as

$$
\mathrm{d}\xi = \rho_e\mu_e U_e\,\mathrm{d}x, \quad \mathrm{d}\eta = \frac{\bar{\rho}U_e}{\sqrt{\xi}}\,\mathrm{d}y. \quad (2.3a,b)
$$

The continuity equation is then eliminated and the transformed momentum and energy equations are

$$
\xi\left(F\frac{\partial F}{\partial\xi} - \frac{\partial F}{\partial\eta}\frac{\partial\Pi}{\partial\xi}\right) = C_1\frac{\partial^2 F}{\partial\eta^2} + \left(\frac{\partial C_1}{\partial\eta} + \frac{\Pi}{2}\right)\frac{\partial F}{\partial\eta} + (G - F^2)\frac{\xi}{U_e}\frac{\mathrm{d}U_e}{\mathrm{d}\xi}, \quad (2.4a)
$$

$$
\xi\left(F\frac{\partial G}{\partial\xi} - \frac{\partial\Pi}{\partial\xi}\frac{\partial G}{\partial\eta}\right) = C_2\frac{\partial^2 G}{\partial\eta^2} + \left(\frac{\partial C_2}{\partial\eta} + \frac{\Pi}{2}\right)\frac{\partial G}{\partial\eta} + Ec_e C_1\left(\frac{\partial F}{\partial\eta}\right)^2, \quad (2.4b)
$$

where the normalized streamwise velocity and temperature are $F = \tilde{U}/U_e$ and $G = \tilde{T}/T_e$ and $\Pi = \int F\,\mathrm{d}\eta$. The other parameters are $C_1 = \bar{\rho}(\tilde{\mu} + \mu_t)/(\rho_e\mu_e)$, $C_2 = \bar{\rho}(\tilde{\kappa} + \kappa_t)/(\rho_e c_p\mu_e)$ and the Eckert number $Ec_e = U_e^2/(c_p T_e)$. The streamwise pressure gradient is reflected in $\mathrm{d}U_e/\mathrm{d}\xi$ through the Bernoulli equation, taken to be zero in the flows considered. The wall-normal boundary conditions at the wall and in the free stream are

$$
\left.
\begin{aligned}
&F = 0, \quad G = T_w/T_e \text{ (isothermal) or } \partial G/\partial\eta = 0 \text{ (adiabatic)}, && \text{at } \eta = 0, \\
&F \to 1, \quad G \to 1, && \text{at } \eta \to \infty.
\end{aligned}
\right\} \quad (2.5)
$$

Equation (2.4) is solved using the streamwise marching procedure (Blottner 1963; Chen, Wang & Fu 2021). At $\xi = 0$, (2.4) degenerates into two ODEs in terms of η, which are solved using the shooting method and serve as the initial profile. Afterwards, the solution at $\xi > 0$ is feasible through streamwise marching. The streamwise (ξ) derivatives

are discretized using the third-order finite-difference scheme. The Chebyshev collocation method is adopted for the wall-normal direction (η), with more points clustering near the wall. A grid number $N_y = 241$ is adequate to provide grid-independent results. A uniform ξ mesh is adopted, while the grid with increasing spacing can be used for better robustness. At each ξ_i, Newtonian iteration is used for quick convergence of the nonlinear equations. Second-order convergence can be realized for laminar flows (e.g. Chen, Wang & Fu 2022*a*), while for turbulent flows here, the derivatives of μ_t and κ_t may not be smooth (due to the maximum and intersection functions, see § 2.3), so the convergence is only first order. The convergence criterion for $[F, G]^{\mathrm{T}}$ is set to 10^{-9} and at most 50 iterations are allowed at each streamwise location. The above procedure is substantially more efficient than solving (2.1). For the cases in table 1, the mean flow at the target x can be obtained within minutes on a desktop computer. The solver is verified (detailed in Appendix A) through comparing with Hendrickson *et al.* (2023), who solved the full Navier–Stokes (NS) equation with BL models using the US3D code.

It is worth mentioning that μ_t and κ_t from the BL model are zero at $\xi = 0$ (since $y = 0$), so the initial profile at $\xi = 0$ is exactly the laminar counterpart. Thereby, there is a numerical (not physical) transition process downstream as μ_t increases. If the transition is not desirable, the start point for marching ξ_0 can be placed somewhere downstream, where the maximum μ_t/μ_∞ is already high and the flow is turbulent. The initial profile at $\xi_0 > 0$ can still be obtained by solving the ODEs with the streamwise derivatives (left-hand sides in (2.4)) artificially dropped. The regime of streamwise adjustment is short due to the parabolic nature of (2.2), so the results downstream are not sensitive to ξ_0.

2.3. *Baseline BL model*

As mentioned in § 1, the BL model using semilocal units for the inner layer construction outperforms the one using wall-viscous units in high-speed applications (Dilley & McClinton 2001). Therefore, the semilocal version is selected as the baseline BL model for modification. For future reference, it is termed the BL-local model in this work. The formulations are specified below, primarily following Cheatwood & Thompson (1993) for the LAURA code. The two-layer formulation of μ_t in BL (and also CS) is

$$\mu_t = \begin{cases} \mu_{t,i}, & y \le y_{m\mu}, \\ \mu_{t,o}, & y > y_{m\mu}, \end{cases} \tag{2.6}$$

where $y_{m\mu}$ is the matching (intersection) point between the inner layer $\mu_{t,i}$ and outer layer $\mu_{t,o}$. The former is based on the mixing length concept, as

$$\mu_{t,i} = \bar{\rho} l_{mix}^2 |\tilde{\omega}|, \quad l_{mix} = \kappa_c y \left[1 - \exp\left(-\frac{y^*}{A^+}\right) \right], \quad A^+ = \frac{26}{\sqrt{|\bar{\tau}^+|}}, \tag{2.7a–c}$$

where $\tilde{\omega}$ is the vorticity, l_{mix} is the mixing length corrected by the exponential damping function of van Driest (1956) and κ_c is the von Kármán constant, taken as 0.40. There are two differences in (2.7*a–c*) from the original version of Baldwin & Lomax (1978). First, y^* is used in the exponent of l_{mix}, instead of y^+, which was also adopted in recent works on WMLES (Yang & Lv 2018; Fu, Bose & Moin 2022; Kamogawa, Tamaki & Kawai 2023). Second, A^+ is not a constant, but dependent on the local total shear $\bar{\tau}^+ = \bar{\tau}/\tau_w$. For thin layer flows, $|\tilde{\omega}|$ can be simplified to $|\partial \tilde{U}_{/\!/}/\partial n|$, where $\tilde{U}_{/\!/}$ is the velocity parallel to the wall, and n is the wall-normal direction. For the configurations in figure 1, we simply have $|\tilde{\omega}| = |\partial \tilde{U}/\partial y|$.

The outer-layer viscosity is evaluated by the Clauser–Klebanoff formulation (Klebanoff 1955; Clauser 1956). First, Clauser reasoned that for boundary layers, the eddies sufficiently away from the wall are no longer constrained by the wall, so their sizes should be proportional to the overall boundary layer thickness. The resulting maximum kinematic eddy viscosity in the outer layer is $\nu_{t,max} \sim U_e \delta_k^*$, or $\nu_{t,max} = \alpha U_e \delta_k^*$, where $\delta_k^* = \int (1 - \tilde{U}/U_e)\, dy$ is the kinematic displacement thickness (equals the displacement thickness in incompressible cases) and α is a closure coefficient. Farther away from the wall, the flow becomes intermittent. An empirical intermittency factor F_{Kleb} (specified later) was introduced by Klebanoff, to model the diminishing of $\nu_{t,o}$ with increasing height. Consequently, $\mu_{t,o}$ is computed as $\bar{\rho}\nu_{t,max}F_{Kleb}$, which leads to the prevailing CS model. To avoid determining the boundary layer thicknesses, which is beneficial for complex flows, $U_e \delta_k^*$ in $\nu_{t,max}$ is replaced by the wake function $C_{cp}y_{max}F_{max}$ in the BL model, which can be justified from the defect velocity scaling (detailed in § 3.2). Therefore, the outer-layer μ_t, adopted without explicit compressible corrections, is

$$\mu_{t,o} = \bar{\rho}\alpha C_{cp}y_{max}F_{max}F_{Kleb}, \tag{2.8}$$

where the vorticity function and the intermittency function are

$$F_{max} = \frac{1}{\kappa_c} \max_{y=y_{max}} (l_{mix}\,|\tilde{\omega}|)\,, \quad F_{Kleb}\left(\frac{y}{y_{max}}\right) = \left[1 + 5.5\left(C_{Kleb}\frac{y}{y_{max}}\right)^6\right]^{-1}. \tag{2.9a,b}$$

Notably, y_{max} is the peak position of the vorticity function following common usage, not the height of the computational domain. Compared with the CS model, the boundary layer thickness in F_{Kleb} is replaced by y_{max}/C_{Kleb}. For more general flows, $\mu_{t,o}$ can be further restricted by a wake relation designed for free shear flows (see Wilcox 2006). It is inactive in the present wall-bounded cases, thus not displayed for conciseness.

Besides κ_c and A^+, there are three closure coefficients α, C_{cp} and C_{Kleb} in the baseline model. Some works (e.g. Gupta *et al.* 1990) suggest their *Ma* dependence, but following the principles in § 1, we adopt the original constant values, $\alpha = 0.0168$, $C_{cp} = 1.6$ and $C_{Kleb} = 0.3$. After the numerical discretization, the intersection and maximum operations in (2.6) and (2.9a,b) are conducted after a third-order interpolation on adjacent grid points, to ensure smoothness and accuracy. After obtaining μ_t, $\kappa_t = c_p\mu_t/Pr_t$ is calculated through a prescribed Pr_t. Although Pr_t can be designed as a function of the wall-normal height (Subbareddy & Candler 2012), the simplest choice of a constant Pr_t is adopted, equal to 0.9 as a common choice. The effects of Pr_t variations will be discussed in § 3.3.

Two cases are employed to demonstrate the behaviour of the baseline BL-local model. First is an incompressible case from SO (Ma_∞ set to 0.01 in our solver). The mean velocity and eddy viscosity are compared with the DNS data at $Re_\theta = 2540$ in figure 2. Note that μ_t from DNS is evaluated by definition as $\mu_t = -\bar{\rho}\widetilde{u''v''}/(\partial\tilde{U}/\partial y)$; μ_t near the boundary layer edge is not displayed since both the numerator and denominator tend to zero. The predicted streamwise velocity is basically in line with DNS, showing the good capability of BL for incompressible flows. In the inner layer, μ_t^+ faithfully follows the incompressible scaling by Johnson & King (1985) as

$$\nu_{t,i}^+ = \kappa_c y^+ \left[1 - \exp\left(-\frac{y^+}{17}\right)\right]^2, \tag{2.10}$$

where the last multiplier is termed the damping function. Note that (2.10) is more convenient than (2.7a–c) for comparisons between cases because $\tilde{\omega}$ does not explicitly appear. Away from the wall, the damping function is nearly unity, so the
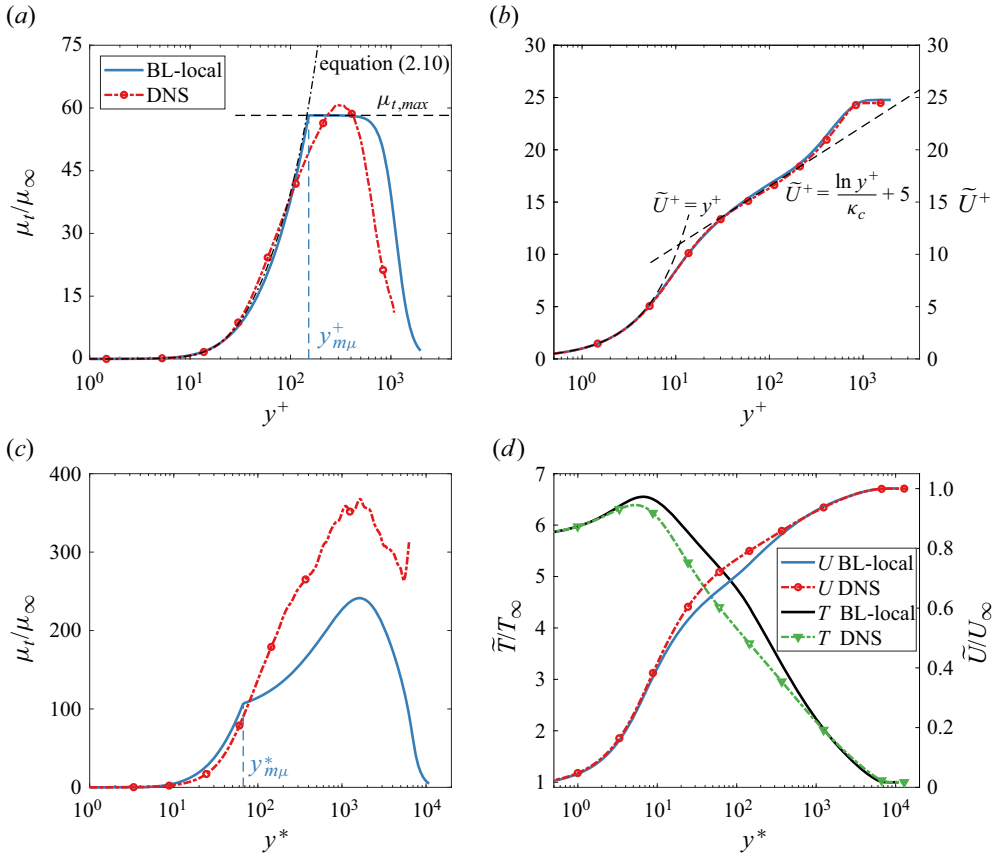
Figure 2. (*a,c*) Eddy viscosity and (*b,d*) mean streamwise velocity and temperature (only compressible case) from the baseline BL-local model and DNS for the (*a,b*) incompressible SO-M0R25 case and (*c,d*) hypersonic ZDC-M8Tw048R20 case.

logarithmic scaling is formulated. In the outer layer, the peak value $\mu_{t,max} = \bar{\rho}\nu_{t,max}$ from the BL model is also close to the DNS (note that $\bar{\rho}$ is invariant), so the matching point $y_{m\mu}^{+} = 152$ ($y_{m\mu} = 0.18\delta_{99}$) is near the upper bound of the logarithmic region, above which the outer-layer scaling is formulated. Although $\mu_{t,o}$ damps (by F_{Kleb}) more slowly than the DNS in the intermittent region, only a minor difference in $\tilde{U}$ appears due to the diminishing $\partial\tilde{U}/\partial y$.

For the hypersonic cold-wall case M8Tw048R20 from ZDC, however, $\tilde{U}$ and $\tilde{T}$ from the BL-local model have clear deviations from the DNS data, especially for $\tilde{T}$, as shown in figure 2(*d*). The discrepancy can be explained from figure 2(*c*). Compared with DNS, $\mu_{t,o}$ is severely underestimated, so the matching point $y_{m\mu}^{*} = 67$ ($y_{m\mu} = 0.09\delta_{99}$) is quite low. Consequently, the region $67 < y^{*} \lesssim 300$ ($0.09 < y_{m\mu}/\delta_{99} \lesssim 0.27$) is not formulated by the logarithmic scaling in (2.7*a*), leading to the errors in $\tilde{U}$ and $\tilde{T}$ there. Meanwhile, $\tilde{T}$ around the temperature peak ($y^{*} \sim 7$) is over-predicted, possibly due to the inaccurate Pr_t there (specified in § 3.3).

987 A7-10

In the following, the inner and outer-layer scalings of μ_t and κ_t are investigated separately using the DNS data. Three targeted modifications are proposed based on established relations.

3. Established relations and *a priori* examination

3.1. *Inner-layer scaling*

First, we demonstrate that the formulation of $\mu_{t,i}$ in the BL-local model is equivalent to applying the TL transformation. Analogous derivation was presented by Yang & Lv (2018) within the WMLES framework. Using the definition of μ_t and (2.7a–c), the mixing-length relation can be expressed, in wall-viscous units, as

$$-\bar{\rho}^+\widetilde{u''^+v''^+} = \bar{\rho}^+ l_{mix}^{+2}\left|\frac{\partial \tilde{U}^+}{\partial y^+}\right|^2 = \bar{\rho}^+\left|\frac{\partial \tilde{U}^+}{\partial y^+}\right|^2 \kappa_c^2 y^{+2}\left[1 - \exp\left(-\frac{y^*}{A^+}\right)\right]^2. \quad (3.1)$$

The left-hand side, $-\bar{\rho}^+\widetilde{u''^+v''^+} = -\overline{\rho u''v''}/\tau_w = -\widetilde{u''^*v''^*}$, is the density-weighted or semilocal Reynolds shear stress (Morkovin's scaling), which is known to well match the incompressible counterpart in the inner layer in terms of y^* (Coleman *et al.* 1995; Pirozzoli & Bernardini 2011; Zhang *et al.* 2018; Hirai, Pecnik & Kawai 2021; Cheng & Fu 2022; Cogo *et al.* 2022; Bai *et al.* 2023). Meanwhile, it is recognized that the right-hand side is related to the TL transformation, $U_{TL}^+(y^*) = \int \bar{\mu}^+(\partial y^*/\partial y^+)\,\mathrm{d}\bar{U}^+$. The resulting form, under the notation of Favre averages, is

$$-\bar{\rho}^+\widetilde{u''^+v''^+} = \left|\frac{\partial U_{TL}^+}{\partial y^*}\right|^2 \kappa_c^2 y^{*2}\left[1 - \exp\left(-\frac{y^*}{A^+}\right)\right]^2. \quad (3.2)$$

The left-hand side and right-hand side are both functions of y^*, so if the transformed inner layer shear well matches the incompressible counterpart, then (2.7a) will be a highly accurate modelling of $\mu_{t,i}$. For diagnostic purposes, a semilocal eddy viscosity is defined as

$$\mu_{t,TL}^*(y^*) = \frac{-\bar{\rho}^+\widetilde{u''^+v''^+}}{\partial U_{TL}^+/\partial y^*} = \frac{\mu_t}{\tilde{\mu}}, \quad (3.3)$$

which is expected to match the incompressible $\mu_{t,i}$ (or $\nu_{t,i}$). Equation (3.3) is examined in figure 3(*a*) using all the DNS data in table 1. Since we are concerned with the inner layer part, $\mu_{t,TL}^*$ is plotted in dotted lines after reaching its maximum. The reference line is the counterpart of (2.10) with y^+ replaced by y^* (Yang & Lv 2018), as

$$\mu_{t,i}^* = \kappa_c y^*\left[1 - \exp\left(-\frac{y^*}{17}\right)\right]^2. \quad (3.4)$$

There is only a small scattering of $\mu_{t,TL}^*(y^*)$ within and below the buffer layer, showing the accuracy of the TL transformation for that region. This also explains the well-predicted surface quantities in the BL-local model for hypersonic cases (Dilley & McClinton 2001). In the logarithmic region, $\mu_{t,TL}^*$ tends to be lower than (3.4), especially for diabatic cases, suggesting an underestimated $\mu_{t,i}$ in BL-local. This is consistent with the behaviour of U_{TL}^+, which can lead to over-prediction in the logarithmic region in diabatic cases. Nevertheless, figure 2(*c*) indicates that $\mu_{t,i}$ in the BL-local model is somewhat higher than DNS, rather than lower. This inconsistency is due to the discrepancy in $\tilde{T}$, on which the variables for constructing the semilocal units ($\bar{\rho}$ and $\tilde{\mu}$) are dependent.
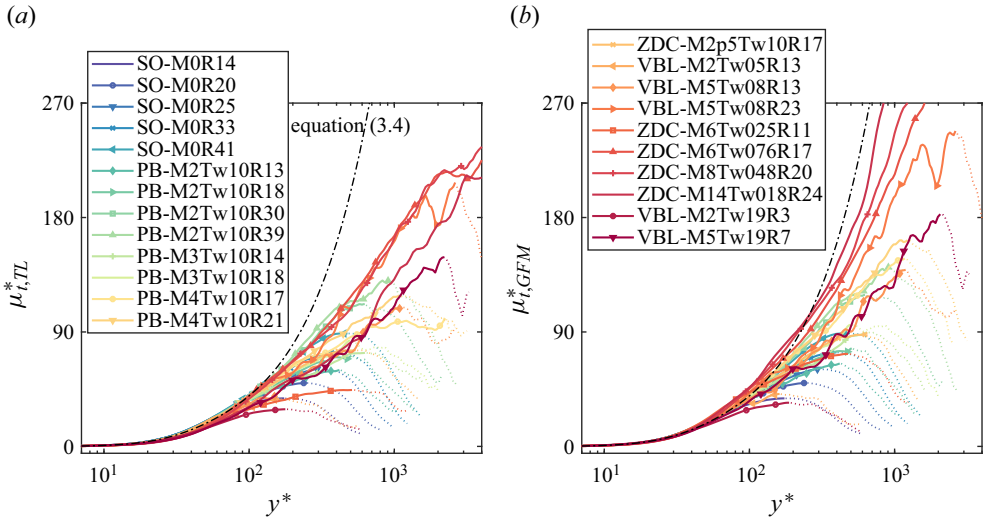
Figure 3. Semilocal eddy viscosity using the (*a*) TL (as in the BL-local model) and (*b*) GFM transformations from the DNS datasets. The legends for panels (*a*,*b*) are the same, separately shown in the two boxes.

As an alternative, we employ the GFM transformation to construct $\mu_{t,i}$, a thought recently implemented by Griffin *et al.* (2023) and Hendrickson *et al.* (2023) for model improvement. The results using the very recent HLPP transformation will be discussed in Appendix B. The GFM is shown to have better overall performances than TL for canonical air flows, particularly diabatic boundary layers in the logarithmic layer, though it can degrade for supercritical or non-air-like flows (Bai *et al.* 2022; Hasan *et al.* 2023*b*). This transformation is defined as

$$U_{GFM}^+(y^*) = \int_0^{y^*} S_t^+ \, \mathrm{d}y^*, \quad S_t^+ = \frac{S_{eq}^+}{1 + S_{eq}^+ - S_{TL}^+} = \frac{\dfrac{1}{\tilde{\mu}^+}\dfrac{\partial \tilde{U}^+}{\partial y^*}}{1 + \dfrac{1}{\tilde{\mu}^+}\dfrac{\partial \tilde{U}^+}{\partial y^*} - \tilde{\mu}^+\dfrac{\partial \tilde{U}^+}{\partial y^+}},$$

(3.5*a*,*b*)

where S_{TL}^+ is the TL transformation kernel defined above, and S_{eq}^+ results from the approximate balance of turbulence production and dissipation in the logarithmic region, as a modification to the arguments of Zhang *et al.* (2012). Similar to (3.2), the GFM-based mixing length relation in the semilocal coordinate takes the form of

$$-\bar{\rho}^+ \widetilde{u''^+ v''^+} = \left|\frac{\partial U_{GFM}^+}{\partial y^*}\right|^2 \kappa_c^2 y^{*2} \left[1 - \exp\left(-\frac{y^*}{A^+}\right)\right]^2.$$

(3.6)

Accordingly, the semilocal eddy viscosity using GFM is

$$\mu_{t,GFM}^*(y^*) = \frac{-\bar{\rho}^+ \widetilde{u''^+ v''^+}}{\partial U_{GFM}^+/\partial y^*} = \frac{\mu_t}{\tilde{\mu}}\frac{\partial U_{TL}^+/\partial y}{\partial U_{GFM}^+/\partial y}.$$

(3.7)

As shown in figure 3(*b*), $\mu_{t,GFM}^*$ experiences smaller scattering than $\mu_{t,TL}^*$ at $y^* \lesssim 70$. Also, $\mu_{t,GFM}^*$ in the logarithmic region follows (3.4) more closely, demonstrating better robustness for modelling $\mu_{t,i}$ than (2.7*a*). For practical use, the incompressible analogy

987 A7-12

$\mu^*_{t,GFM}$ is computed first using (3.6), based on y^* and $\partial U^+_{GFM}/\partial y^*$; afterward, $\mu_{t,i}$ is obtained from (3.7).

Notably, the GFM and TL transformations are designed only for the region within and below the logarithmic layer, so their accuracy for the outer region is not guaranteed. Consequently, they may not be directly used to modify the outer-layer μ_t. Our exploration to improve the $\mu_{t,o}$ modelling is presented below.

3.2. *Outer-layer scaling*

The derivation of the outer-layer scaling in the baseline BL model is briefly reviewed first, to set the grounds for possible modifications.

The crucial part of modelling $\mu_{t,o}$ is the estimation of its peak value, as learned from figure 2. In (2.8), the peak value $\nu_{t,max}$ is estimated first, then $\mu_{t,o}$ is formed as $\bar{\rho}\nu_{t,max}$ before the diminishing by F_{Kleb}. Consequently, $\mu_{t,o}$ can continue to increase at $y > y_{m\mu}$ due to the rising $\bar{\rho}$ (see figure 2c), rather than monotonically decreasing as in incompressible cases. Therefore, it is first a question whether $\nu_{t,max}$ (then $\mu_{t,o} = \bar{\rho}\nu_{t,max}F_{Kleb}$, as in BL-local) or $\mu_{t,max}$ (the maximum μ_t, then $\mu_{t,o} = \mu_{t,max}F_{Kleb}$ which monotonically decreases with y) should be modelled. In hypersonic cases, $\bar{\rho}$ can vary considerably in the outer region, so the two strategies can lead to significant differences. From existing works, the scaling for $\mu_{t,max}$ is scarce while that for $\nu_{t,max}$ is prevailing, so the following investigation is mainly on $\nu_{t,max}$. As mentioned in §2.3, Cebeci & Smith (1974) argued that $\nu_{t,max}$ was proportional to the boundary layer thickness, and suggested two scalings,

$$\nu_{t,max} = \alpha U_e \delta^*_k = \alpha \nu_e Re_{\delta^*_k} \quad \text{and} \quad \nu_{t,max} = \alpha_2 u_\tau \delta_{99} = \alpha_2 \nu_w Re_\tau, \qquad (3.8a,b)$$

which also hold in compressible flows. The first closure constant α has been introduced in §2.3, and the second one α_2 is 0.06–0.075. Although widely used, (3.8) is re-examined here using the DNS data for future reference. The ratios $\alpha_{2,DNS} = \nu_{t,max}/(u_\tau \delta_{99})$ and $\alpha_{DNS} = \nu_{t,max}/(U_e \delta^*_k)$ for all cases are shown in figure 4(a,b), as functions of the corresponding Reynolds numbers. For incompressible cases, $\alpha_{2,DNS}$ varies more slightly than α_{DNS} with increasing Re. When compressible cases are included, however, $\alpha_{2,DNS}$ is the less robust one. In particular, $\alpha_{2,DNS}$ varies more than twice between the diabatic cases, which is not surprising due to its higher sensitivity to wall quantities by definition.

For incompressible flows, the well-known velocity defect law provides another way to estimate $\nu_{t,max}$ without using the boundary layer thicknesses, as adopted in the BL model. Specifically, the Clauser defect law reads $U^+_e - \tilde{U}^+ = U^+_{df}(\eta)$, where U^+_{df} is the defect velocity and the outer scale $\eta = y/\Delta$ is based on the Rotta–Clauser boundary layer thickness $\Delta = U^+_e \delta^*_k = \int (U^+_e - \tilde{U}^+) \, \mathrm{d}y$ (note that η is no longer the transformed coordinate defined in §2.2). Consequently, a collapse of the following function is suggested as

$$-\eta \frac{\mathrm{d}U^+_{df}}{\mathrm{d}\eta} = \eta \frac{\partial \tilde{U}^+}{\partial \eta} = y \frac{\partial \tilde{U}^+}{\partial y} \approx \frac{l_{mix}}{\kappa_c} \frac{\partial \tilde{U}^+}{\partial y} = \frac{l_{mix} |\tilde{\omega}|}{\kappa_c u_\tau}, \qquad (3.9)$$

where the approximation holds in the outer layer where $y^* \gg A^+$ (see (2.7c)). The last term is the scaled vorticity function in (2.9a), and the first three terms are the diagnostic function commonly used to evaluate κ_c, though the main focus here is on the outer layer. For a quantitative evaluation of (3.9) and then $y_{max}F_{max}$, the semiempirical relation by Monkewitz, Chauhan & Nagib (2007) for incompressible boundary layers in the large-Re limit is employed, which gives one explicit expression of $U^+_{df}(\eta)$. As a result,
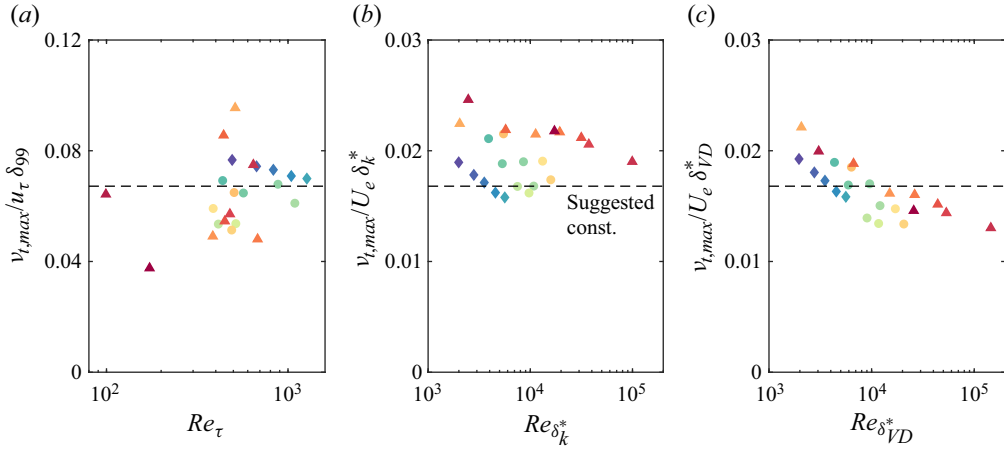
Figure 4. Maximum kinematic eddy viscosity scaled by different variables (see (3.8*a,b*) and (3.11)) from the DNS data. The diamonds are for incompressible cases, and the cycles and triangles are for adiabatic and diabatic ones, respectively. The symbol colours follow the usage in figure 3.

the outer-layer maximum of $y\partial\tilde{U}^+/\partial y$ is equal to 5.55 at $\eta = 0.155$. Therefore, the ratio of $\nu_{t,max}$ to $y_{max}F_{max}$ using (3.8*a*), i.e.

$$\frac{\nu_{t,max}}{\alpha y_{max}F_{max}} = \frac{U_e\delta_k^*}{0.155U_e^+\delta_k^* \times 5.55u_\tau} = \frac{1}{0.155 \times 5.55}, \qquad (3.10)$$

is a constant (namely C_{cp}, though not exactly the same value), which leads to (2.8) directly used in the compressible baseline BL model. Analogously, if $\nu_{t,max}$ is from (3.8*b*), then the constant in (3.10) can be obtained from another form of incompressible defect law $U_e^+ - \tilde{U}^+ = U_{df}^+(y/\delta_{99})$. Inspired by (3.9) and (3.10), the compressible defect velocity scalings and their derivatives are examined below, to explore possible compressible corrections to (2.8).

As introduced in § 1, most of the existing compressible defect velocity scalings are based on the VD transformation. The VD is built upon the mixing length assumption for the region within and below the logarithmic layer, so the outer layer is not the targeted region for it to work, like other transformations (TL, GFM, etc.). Nevertheless, previous investigations actively support its usage for compressible defect velocity scalings (Maise & McDonald 1968; Fernholz & Finley 1980; Guarini *et al.* 2000; Pirozzoli *et al.* 2004; Duan *et al.* 2011; Pirozzoli & Bernardini 2011; Wenzel *et al.* 2018), suggesting its fundamentality in transforming compressible flows, though the diabatic cases are somewhat insufficiently examined. Therefore, the VD transformation is considered until future reports of more advanced ones. Following the incompressible procedures above, a VD-based displacement thickness can be defined, following Smits & Dussauge (2006), as

$$\delta_{VD}^* = \int_0^\infty \left(1 - \frac{U_{VD}}{U_{VD,e}}\right) \mathrm{d}y, \quad \text{where } U_{VD}^+(y^+) = \int_0^{\tilde{U}^+} \sqrt{\bar{\rho}^+} \, \mathrm{d}\tilde{U}^+. \qquad (3.11)$$

The corresponding outer scale is $\eta_{VD} = y/\Delta_{VD}$, where the transformed Rotta–Clauser thickness is $\Delta_{VD} = U_{VD,e}^+\delta_{VD}^* = \int(U_{VD,e}^+ - U_{VD}^+)\,\mathrm{d}y$. Since VD may not be accurate enough in the inner layer, the transformed displacement thickness can be alternatively defined in a mixed manner, δ_{mix}^*, where the integrand in the inner region (say $y < 0.15\delta_{99}$)

987 A7-14

is replaced by the TL- or GFM-based defect velocity. Taking GFM as an example, the difference between δ_{mix}^* and δ_{VD}^* turns out to be less than 2.5 % and 4.5 % for the supersonic and hypersonic cases, respectively. Since δ_{VD}^* is not finally used in the new model but to inform modification, we employ δ_{VD}^* instead of δ_{mix}^* hereafter for simplicity and consistency. Similar to (3.8), $\nu_{t,max}$ can be evaluated as $\nu_{t,max} = \alpha_{VD} U_e \delta_{VD}^* = \alpha_{VD} \nu_e Re_{\delta_{VD}^*}$, which is examined in figure 4(*c*) by computing $\alpha_{VD,DNS} = \nu_{t,max}/(U_e \delta_{VD}^*)$ for all cases. The ratio $\alpha_{VD,DNS}$ experiences a comparably small variation with α_{DNS}. Besides, there is generally a decreasing trend of $\alpha_{VD,DNS}$ with $Re_{\delta_{VD}^*}$ rising, which awaits future examination using higher-*Re* data. Notably, the diabatic cases exhibit no larger departure than the incompressible and adiabatic cases, though the VD transformation tends to deteriorate. A possible reason is that (3.11) is defined in an integral manner, allowing error cancellation.

Afterwards, the compressible defect velocity scalings are studied, to establish connections with the vorticity function. The form examined by Pirozzoli & Bernardini (2011) for supersonic adiabatic boundary layers is $(U_{VD,e} - U_{VD})/U_{VD,e} = g_1(y/\delta_{99})$, where g_1 is a universal function. This function is computed in figure 5(*c*) for all the DNS cases, and the results before the VD transformation are plotted in figure 5(*a*) for comparison. As can be seen, g_1 for diabatic cases deviates more significantly from the incompressible counterpart. As an alternative to g_1, the VD-based analogy to the Clauser defect law takes the form of $U_{VD,e}^+ - U_{VD}^+ = g_2(\eta_{VD})$, which is examined in figure 5(*b*) between cases. For the present datasets, g_2 tends to achieve a somewhat better collapse than g_1. We proceed to study the derivatives of these defect velocities, to connect with the diagnostic function and then the vorticity function. The diagnostic function used in (2.8) is displayed in figure 5(*d*), where a few strongly oscillating curves are not shown. Note that $y\partial \tilde{U}^+/\partial y$ is plotted instead of $y\partial \tilde{U}/\partial y$ for direct connection with $\nu_{t,max}$ (see (3.10), there is a factor u_τ in (3.8) or Δ). The main focus is on the outer layer, so the region $y < 0.15\delta_{99}$ is plotted in dotted lines. If the outer-layer peaks of $y\partial \tilde{U}^+/\partial y$ are collapsed between cases, then the ratio $\nu_{t,max}/(y_{max}F_{max})$ would be nearly invariant, which would then provide a robust modelling for $\mu_{t,o}$, as derived in (3.10) for incompressible cases. First, the incompressible cases in figure 5(*d*) suggest a rough outer-layer similarity at this *Re* range ($Re_\tau \gtrsim 400$, $Re_{\delta_2} \gtrsim 1400$), though the collapse is not as close to perfect as in the large-*Re* limit (Nagib, Chauhan & Monkewitz 2007). For the compressible cases, the peak locations in figure 5(*d*) all concentrate around $0.7\delta_{99}$, but the maximums vary considerably, especially for some cold-wall cases, even if the low-*Re* cases are excluded. Consequently, $\mu_{t,o}$ can be severely under-predicted, as is observed in figure 2(*c*). For the VD-based defect velocity $g_2(\eta_{VD})$, the outer-layer relation analogous to (3.9) is derived as

$$-\eta_{VD}\frac{\mathrm{d}g_2}{\mathrm{d}\eta_{VD}} = y\frac{\partial U_{VD}^+}{\partial y} = \sqrt{\bar{\rho}^+}y\frac{\partial \tilde{U}^+}{\partial y} \approx \sqrt{\bar{\rho}^+}\frac{l_{mix}\,|\tilde{\omega}|}{\kappa_c u_\tau}, \quad \text{where } y^* \gg A^+. \quad (3.12)$$

As noted by Smits & Dussauge (2006), (3.12) indicates a proper velocity scale in the outer layer to be $u_\tau/\sqrt{\bar{\rho}^+}$, which can be used to extend Coles' law of the wake (Maise & McDonald 1968; Huang *et al.* 1993; Hasan *et al.* 2023*a*). Furthermore, the factor $\sqrt{\bar{\rho}^+}$ turns out to be fundamental to account for compressibility effects, and was suggested by Catris & Aupoix (2000) and Otero Rodriguez *et al.* (2018) to improve the eddy viscosity and diffusivity in sophisticated RANS models. The transformed function $y\partial U_{VD}^+/\partial y$ is plotted in figure 5(*e*) in terms of η_{VD}. Although obvious scattering in peak values and locations is still observable, better collapse is attained compared with figure 5(*d*), demonstrating the effectiveness of the VD density weighting.
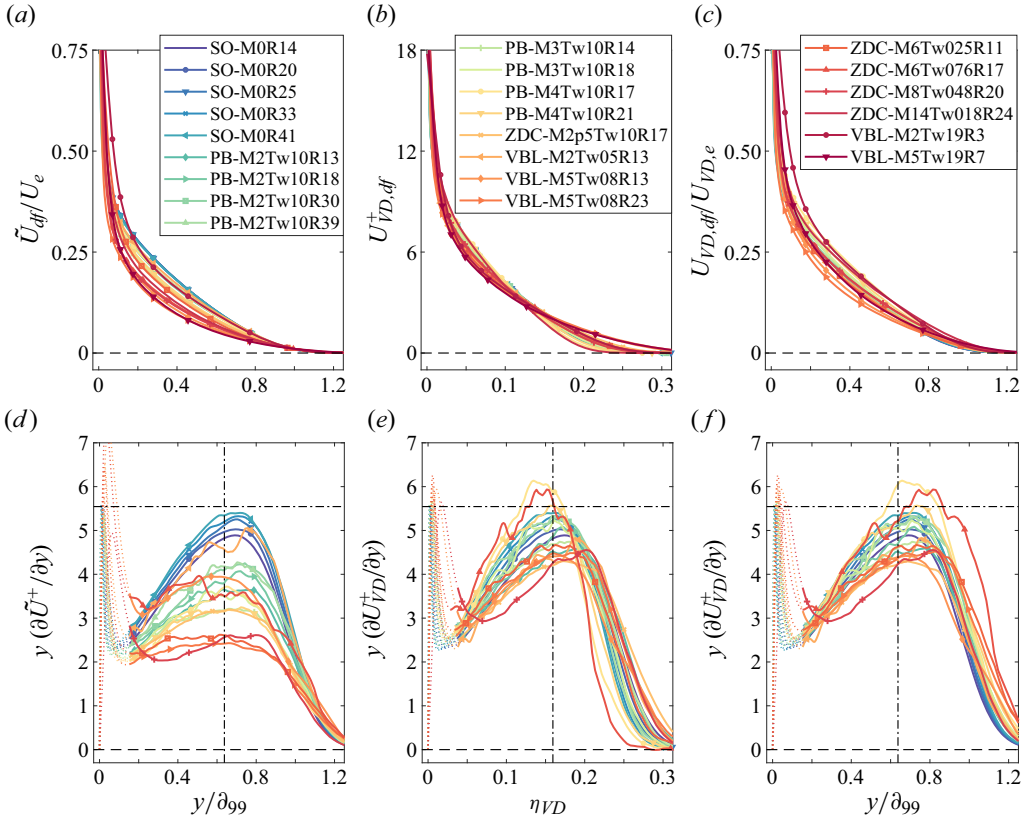
Figure 5. Different forms of (*a–c*) defect velocities and (*d–f*) diagnostic functions for all cases. The reference lines in panels (*d–f*) are from (3.10). The legends for all the panels are the same, separately shown in the three boxes.

Therefore, it is suggested that the VD-based vorticity function can be utilized in the outer layer scaling of the BL model, to replace the original one without compressible corrections. From (3.12), the vorticity function in (2.9*a*) is modified by simply adding a factor $\sqrt{\bar{\rho}^+}$ as

$$F_{VD,max} = \frac{1}{\kappa_c} \max_{y=y_{VD,max}} (\sqrt{\bar{\rho}} l_{mix} |\tilde{\omega}|). \tag{3.13}$$

Here, the denominator $\sqrt{\rho_w}$ has been moved out of this function to combine with other factors in $\mu_{t,o}$, which does not affect the value of $y_{VD,max}$. Consequently, (2.8) is modified to be

$$\mu_{t,o} = \frac{\bar{\rho}}{\sqrt{\bar{\rho}}} \alpha C_{cp} y_{VD,max} F_{VD,max} F_{Kleb} = \sqrt{\bar{\rho}} \alpha C_{cp} y_{VD,max} F_{VD,max} F_{Kleb}. \tag{3.14}$$

Here, the denominator $\sqrt{\bar{\rho}}$ can be interpreted as a compensation to the amplified vorticity function (3.13). The final form also turns out to reach a compromise between the modelling of $\nu_{t,max}$ and $\mu_{t,max}$, so $\mu_{t,o} \sim \bar{\rho}^{1/2} F_{Kleb}$ and $\nu_{t,o} \sim \bar{\rho}^{-1/2} F_{Kleb}$. As a natural consequence, (3.14) produces the same results as (2.8) for incompressible flows with constant density.

The empirical function $F_{Kleb}(y/y_{VD,max})$ remains unmodified as in (2.9*b*) before acquiring more theoretical guidance. Also, the closure constants α, C_{cp} and C_{Kleb}

987 A7-16
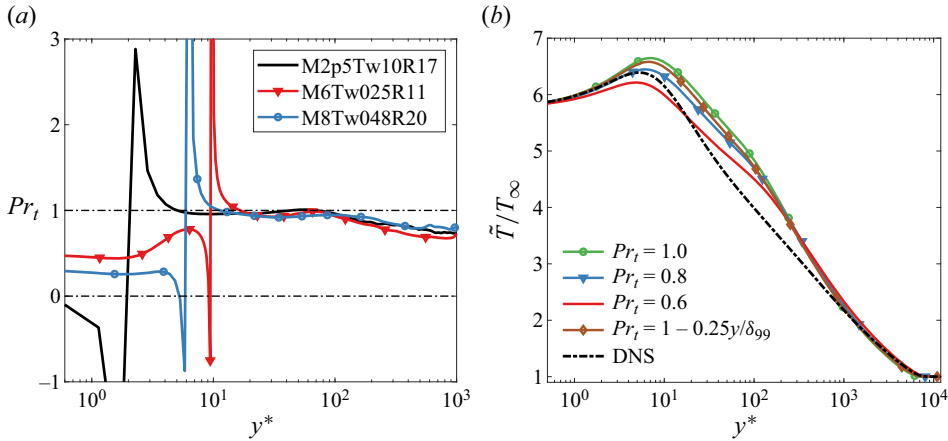
Figure 6. (*a*) Turbulent Prandtl numbers in different DNS cases from ZDC and (*b*) the mean temperature using the BL-local model with different Pr_t for case M8Tw048R20.

remain unaltered, consistent with the incompressible version. Finally, since the quantity $y_{VD,max}/C_{Kleb}$ used in F_{Kleb} represents an estimation of the boundary layer thickness, its relation to δ_{99} is examined in figure 5(*f*) by plotting the transformed function in terms of y/δ_{99}. For most cases, $y_{VD,max}/\delta_{99}$ is within 0.6–0.8, but it seems closer to the boundary layer edge than y_{max}/δ_{99}, suggesting slower damping of $\mu_{t,o}$ in the intermittent region.

3.3. *The TV relation*

As stated in § 2.3, the eddy diffusivity in RANS models for temperature prediction is obtained mostly through a specified Pr_t, whose one common definition is

$$Pr_t = \frac{\widetilde{u''v''}(\partial \tilde{T}/\partial y)}{\widetilde{v''T''}(\partial \tilde{U}/\partial y)}. \tag{3.15}$$

It is widely shown that Pr_t is within 0.7–1.1 in most regions above the buffer layer and is typically equal to 0.85 in the logarithmic region, insensitive to Ma, Re and wall cooling (Huang, Coleman & Bradshaw 1995; Duan *et al.* 2010; Pirozzoli & Bernardini 2011; Lusher & Coleman 2022). However, Pr_t can experience complicated variations within and below the buffer layer, especially in cold-wall boundary layers, which is illustrated in figure 6(*a*) using the DNS data from ZDC. At $y^* \gtrsim 25$, three Pr_t are quite close to each other, slowly decreasing towards the boundary layer edge. Near the temperature peak, however, $\partial \tilde{T}/\partial y$ and $\widetilde{v''T''}$ both change signs, so Pr_t can be negative or even singular. This singularity is also observable in the adiabatic case M2p5Tw10R17, though very close to the wall ($y^* \approx 2$). Meanwhile, Pr_t between the singular point and the wall is generally lower than 0.5 for the three cases. The rapid variation of Pr_t can lead to prediction errors for the temperature peak, as discussed for figure 2(*d*). For further demonstration, figure 6(*b*) compares between three cases with different Pr_t using the BL-local model (case M8Tw048R20). At $y^* \gtrsim 100$, $\tilde{T}$ is quite insensitive to Pr_t but at $y^* \lesssim 100$, a continuous decrease of $\tilde{T}$ is observed with the drop of Pr_t due to enhanced turbulent heat flux. The case $Pr_t = 0.8$ seems to best predict the temperature peak. For the colder-wall case M6Tw025R11, an even lower $Pr_t = 0.6$ is required in a similar test (not shown) to capture reasonably the peak temperature. Therefore, accurate modelling of Pr_t is significant for

near-wall temperature prediction. A constant $Pr_t = 0.9$ can lead to an over-predicted peak temperature for cold-wall cases.

Besides constancy, Pr_t can be modelled as a function of the wall-normal height (Abe & Antonia 2017; Huang, Duan & Choudhari 2022; Huang *et al.* 2023); for example, the expression by Subbareddy & Candler (2012) for boundary layers is $Pr_t = 1 - 0.25y/\delta_{99}$. This formula is also examined in figure 6(*b*) within the BL model. The resulting temperature is close to the $Pr_t = 1$ case and thus inaccurate for near-wall temperature prediction. Other available Pr_t formulae are expected to have analogous behaviours because Pr_t are all designed to monotonically decrease away from the wall, though most of the formulae are modelled based on channel flows. As discussed above, capturing the non-monotonic and singular behaviour of Pr_t near the wall is crucial, but it seems difficult to summarize a universal expression of Pr_t in the near-wall region. The location of the singular point may correlate with the temperature peak, but the Pr_t farther below towards the wall also differs considerably from case to case. *Ad hoc* fitting of Pr_t for each case is plausible, but no universality is guaranteed. Consequently, we seek alternatives to specifying Pr_t. As mentioned in § 1, the algebraic TV relation by Duan & Martín (2011) and Zhang *et al.* (2014) is remarkably accurate for adiabatic and diabatic boundary layers, and channel and pipe flows. It is thus incorporated for efficient and accurate temperature prediction in several recent works within the frameworks of ODE solvers and WMLES (Chen *et al.* 2023*a*; Griffin *et al.* 2023; Hasan *et al.* 2023*a*; Song *et al.* 2023). Thereby, the TV relation is utilized to improve the temperature prediction in the BL model.

The quadratic algebraic relation is written as

$$\tilde{T} = T_w + C_T(T_r - T_w)\left(1 - \frac{\tilde{U}}{\tilde{U}_\delta}\right)\frac{\tilde{U}}{\tilde{U}_\delta} + \left(\tilde{T}_\delta - T_w\right)\left(\frac{\tilde{U}}{\tilde{U}_\delta}\right)^2, \quad (3.16)$$

where $\tilde{U}_\delta$ and $\tilde{T}_\delta$ are the values at the boundary-layer edge δ (specified later), and $T_r = T_\infty(1 + rEc_\infty/2)$ is the recovery temperature with $r = Pr^{1/3}$ the recovery factor. The closure constant C_T is determined to be 0.8259 by Duan & Martín (2011) and is recast as sPr by Zhang *et al.* (2014), where the Reynolds analogy factor s is 1.14 following convention. The examination of (3.16) for the deployed DNS datasets is not presented since it has been extensively verified (e.g. Zhang *et al.* 2018; Modesti & Pirozzoli 2019; Fu *et al.* 2021; Zhang *et al.* 2022; Griffin *et al.* 2023). Its implementation into the model is discussed below. In the works of Song *et al.* (2023), Chen *et al.* (2023*a*) and Hasan *et al.* (2023*a*), (3.16) is used throughout the boundary layer. In comparison, Griffin *et al.* (2023) adopt it only in the near-wall region with the upper boundary condition matched by LES. The latter strategy is preferred for two reasons. First, $\tilde{T}$ in the outer layer is already insensitive to Pr_t and Pr_t also varies mildly. Second, by solving the original energy (2.1*c*) in the outer layer, more flow information is retained, which is more applicable to general flows. To realize the multilayer formulation, a matching location $y_{mT} < \delta$ within the boundary layer is required, above which (2.1*c*) is solved and below which (3.16) is enforced. The resulting temperature formulation is also a two-layer structure, analogous to μ_t in (2.6). The outer boundary condition for (3.16) is now the temperature sample at y_{mT}. To enforce the matching temperature $\tilde{T}_m$ at y_{mT}, the original outer boundary condition $\tilde{T}|_{y=\delta} = \tilde{T}_\delta$ is relaxed, and (3.16) is rewritten, following Griffin *et al.* (2023), to be

$$\tilde{T} = T_w + C_T(T_r - T_w)\left(1 - \frac{\tilde{U}}{\tilde{U}_m}\right)\frac{\tilde{U}}{\tilde{U}_\delta} + \left(\tilde{T}_m - T_w\right)\left(\frac{\tilde{U}}{\tilde{U}_m}\right)^2, \quad \text{at } y < y_{mT}, \quad (3.17)$$

where $\tilde{U}_m$ is the velocity sample at y_{mT}. Within the framework in § 2.2, the energy equation (2.4*b*) with constant Pr_t is solved first throughout the boundary layer. As a second step,

(3.17) is used to update $\tilde{T}$ at $y < y_{mT}$ once within each iteration, based on the quantities at y_{mT} and δ. If solving the full RANS equation (2.1), then (3.17) can be directly imposed during the temporal stepping subject to an appropriate initial field.

Note that only a zero-order continuity of $\tilde{T}$ at y_{mT} is guaranteed by (3.17). Actually, such a high-order discontinuity also exists in μ_t at $y_{m\mu}$ (see figure 2). Numerical results prove negligible effects of the discontinuities on the mean profiles after the computation converges. Inspired by figure 6(b), y^*_{mT} is fixed at 100 throughout. A sensitivity study of y^*_{mT} is conducted in Appendix A, suggesting minor differences in the mean temperature with y^*_{mT} varied from 50 to 150. In the spirit of the BL model, the explicit determination of the boundary layer edge, required by $\tilde{U}_\delta$ and $\tilde{T}_\delta$, should be avoided. Consistent with (2.9a), δ is set to y_{max}/C_{Kleb} ($y_{VD,max}/C_{Kleb}$ if using (3.14)), and the final results turn out to be quite insensitive to δ. As a final remark, (3.17) is designed for fully developed turbulence and becomes invalid for laminar flows (however, see the recent results of Mo & Gao (2024)), so the numerical transition process mentioned in § 2.2 should be avoided; in other words, the initial profile should be placed downstream in the turbulent regime.

3.4. *Modification summary*

As described in §§ 3.1–3.3, three well-established mean flow relations are employed to modify the BL-local model. Two modifications are made to the two-layer μ_t in (2.6). To be specific, the GFM transformation is utilized for the inner layer $\mu_{t,i}$ (3.7), and the VD transformation is adopted for the outer-layer $\mu_{t,o}$ (3.14). This version, without modifying the temperature relation, is termed the BL-GFM-VD model. Furthermore, one modification is made to the inner layer temperature. The algebraic TV relation (i.e. (3.17)) is enforced at $y < y_{mT}$, instead of specifying Pr_t and solving the energy equation. This final version is called the BL-GFM-VD-TV model. For incompressible flows with constant thermodynamic properties, the two modified models (and also BL-local) degenerate to the original version by Baldwin & Lomax (1978).

4. Results of the modified BL models

The two modified BL models are comprehensively evaluated using the 12 DNS cases. The primary quantities of interest are the mean profiles, and the wall and integral quantities. The fluctuation statistics are not expected to agree well with DNS considering the great simplicity in RANS.

The cold-wall Ma8Tw048R20 case from ZDC is focused on first, as examined in figure 2. The mean streamwise velocity and temperature predicted by the three BL models are shown in figure 7 in the inner scale. The distributions of μ_t and Pr_t are also displayed for diagnostic purposes. As mentioned above, the BL-local model underestimates the outer-layer μ_t for this case, leading to a smaller u_τ and an upward tilting of $\tilde{U}^+$ in the outer region, compared with the DNS data. This tilting of $\tilde{U}^+$ suggests an under-predicted $\tilde{U}/U_\infty = \tilde{U}^+/U^+_\infty$ in the logarithmic region, as displayed in figure 2(d). A notable improvement for the outer-layer $\tilde{U}^+$ is observed in the BL-GFM-VD model, and as a step forward, $\tilde{U}^+$ (and also $\tilde{U}/U_\infty$ in the outer scale) from BL-GFM-VD-TV is closely in line with DNS. From figure 7(c), the matching point $y^*_{m\mu} = 242$ ($y_{m\mu} = 0.24\delta_{99}$) is much higher than that in BL-local ($y^*_{m\mu} = 67$ in figure 2c), owing to the lifted $\mu_{t,o}$ after utilizing the VD transformation. Consequently, the region $y^* \lesssim 242$ obeys the logarithmic scaling formulated by the GFM transformation. In tandem with the more accurate $\tilde{U}$, clear
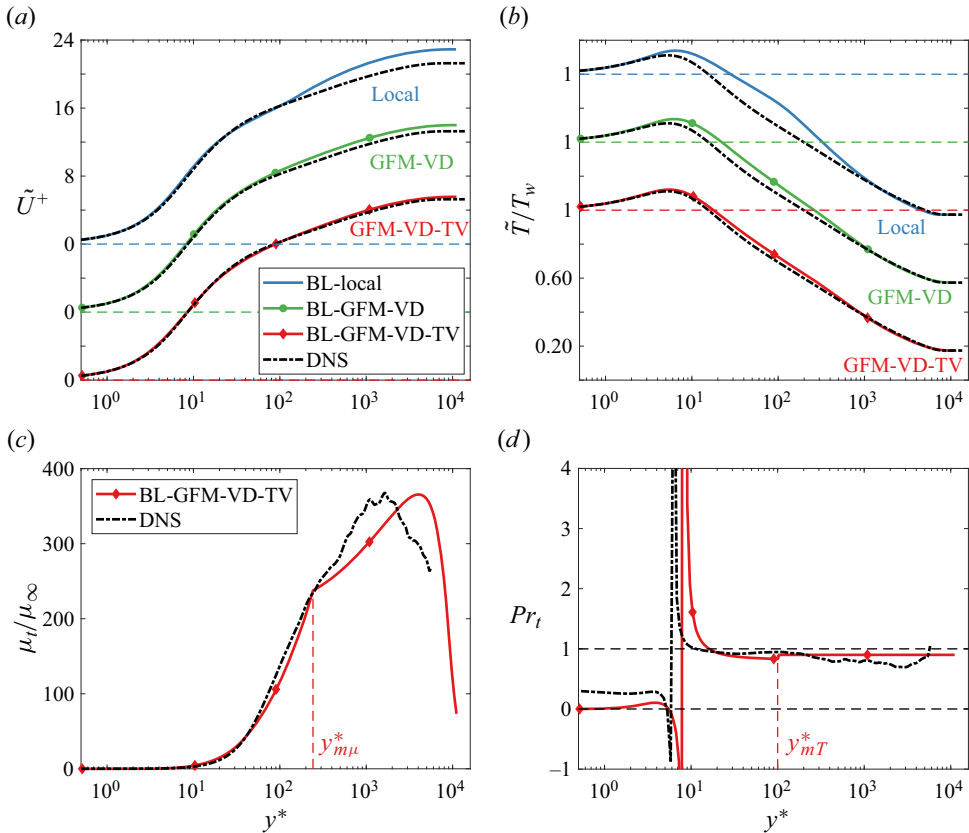
Figure 7. (*a*) Mean streamwise velocity, (*b*) mean temperature, (*c*) eddy viscosity and (*d*) turbulent Prandtl number from different BL models and DNS for case ZDC-Ma8Tw048R20 (cold wall).

improvement in predicting $\tilde{T}$ is observed in figure 7(*b*) from BL-local to BL-GFM-VD. Nevertheless, the predicted peak temperature and that in the logarithmic region are still higher than DNS. Further improvement coinciding with DNS is realized in the BL-GFM-VD-TV model, where the inner layer $\tilde{T}$ is formulated by (3.17). The excellent agreement of $\tilde{T}$ in the BL-GFM-VD-TV model can be explained from *a posteriori* diagnosis of Pr_t, which is computed by substituting the BL results back to the energy equation (2.1*c*) or (2.4*b*). As shown in figure 7(*d*), Pr_t at $y^* > y^*_{mT}$ is 0.9 by construction. At $y^* < y^*_{mT}$, Pr_t is not a constant but varies in a qualitatively consistent manner with DNS; a singular point also appears at $y^* \approx 8$. The slight discontinuity in Pr_t around y^*_{mT} is due to the matching procedure, as noted in § 3.3. In short, by employing the TV relation, the intricate variation of Pr_t near the wall can be modelled, leading to an accurate temperature prediction combined with an appropriate μ_t.

Similar intermodel comparisons are made for the remaining DNS cases. For conciseness, we demonstrate below the mean-flow profiles of three representative cases from different sources: one cold-wall case from ZDC (M6Tw025R11); one adiabatic-wall case from PB (M4Tw10R21); one heated-wall case from VBL (M2Tw19R3). Afterwards, more attention will be paid to diabatic cases, and the prediction errors of the remaining cases will be summarized collectively.

987 A7-20
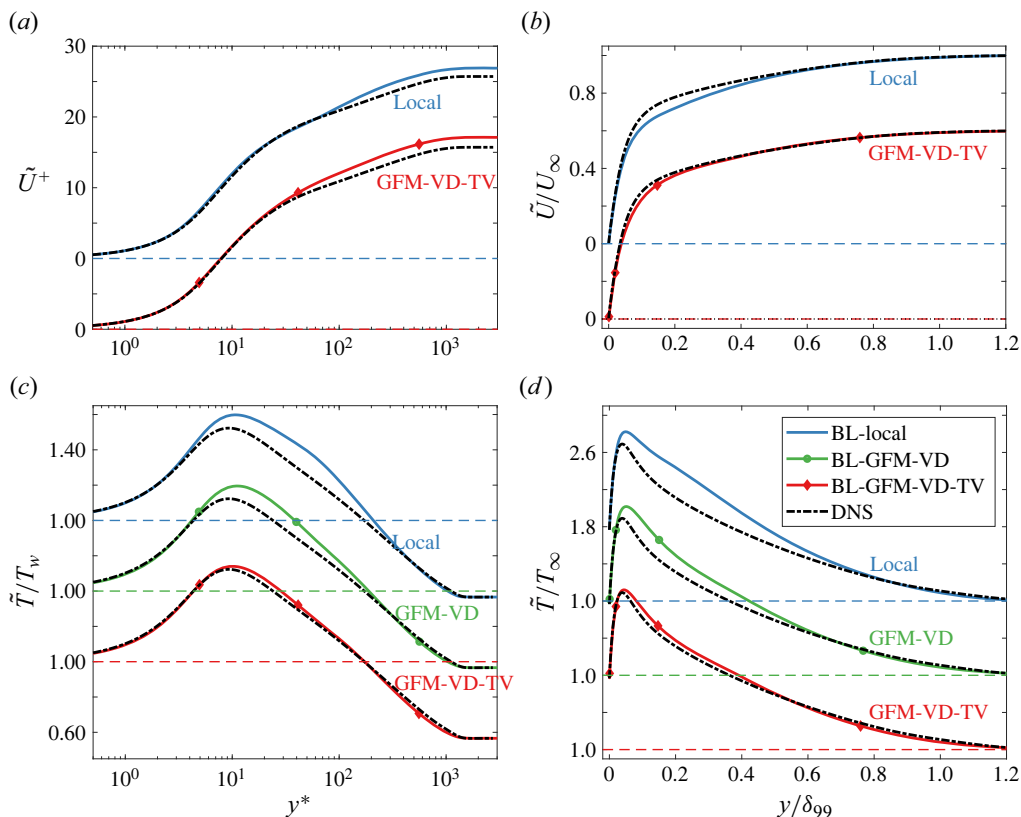
Figure 8. Mean (*a,b*) streamwise velocity and (*c,d*) temperature in the (*a,c*) inner and (*b,d*) outer scales from different BL models for case ZDC-M6Tw025R11 (cold wall).

The results of the cold-wall M6Tw025R11 case are shown in figure 8 in both the inner and outer scales. The velocity prediction from the BL-GFM-VD model is close to BL-GFM-VD-TV, especially in the outer scale, so the former is not displayed. The model comparisons for velocity exhibit different features in the inner and outer scales. Both models tend to under-predict u_τ, thus leading to higher $\tilde{U}^+$ in the outer region; $\tilde{U}^+$ by BL-GFM-VD-TV tends to deviate more. If expressed in the outer scale, nevertheless, $\tilde{U}$ by BL-GFM-VD-TV follows the DNS trend more closely, especially in the logarithmic region due to the elevated $\mu_{t,o}$ and hence a higher $y_{m\mu}$ ($y^*_{m\mu}$ rises from 80 in BL-local to 224). The reversed trends in the inner and outer scales will be revisited later, along with more quantitative measurements of the prediction errors. The temperature predictions of the three BL models strongly resemble those in figure 7. The BL-local model severely over-predicts $\tilde{T}$ in most regions ($y < 0.7\delta_{99}$) within the boundary layer, especially when expressed in the outer scale (figure 8*d*). Though the error in the logarithmic region is reduced in the BL-GFM-VD model owing to the improved logarithmic scaling, clear over-prediction still exists due to the overrated Pr_t in the near-wall region. After employing the TV relation, excellent agreement with DNS is obtained in the BL-GFM-VD-TV model.

The adiabatic case M4Tw10R21 is considered in figure 9. As extensively examined in previous works (see § 1), the BL-local model well reproduces the mean velocity, but $\tilde{T}$ in the logarithmic region is over-estimated. After using BL-GFM-VD and BL-GFM-VD-TV,
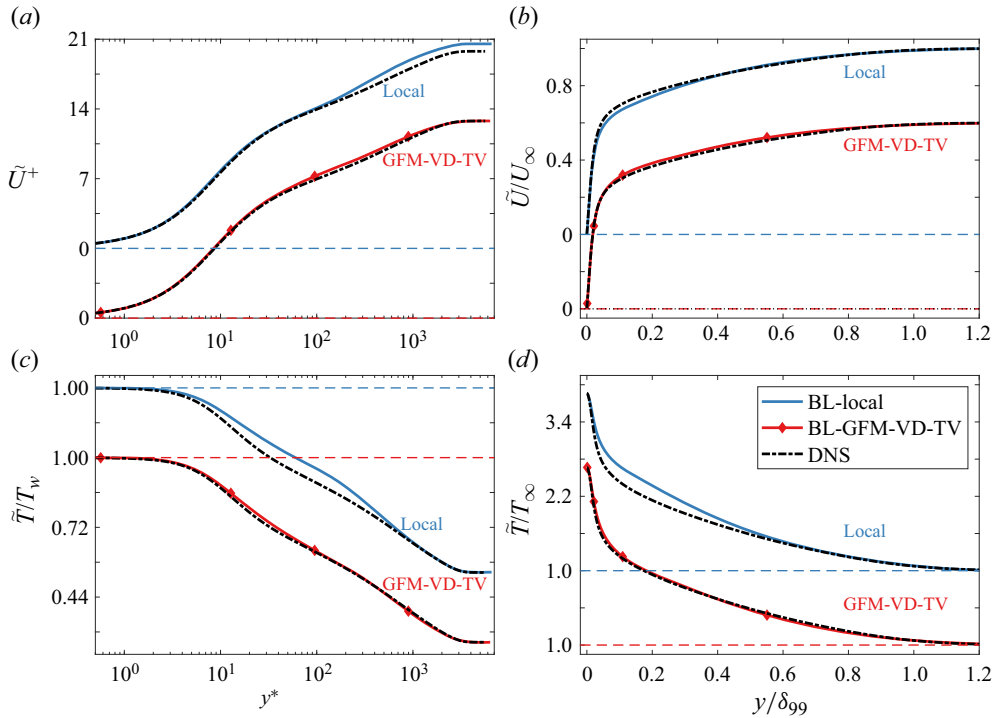
Figure 9. Same as figure 8 except for case PB-M4Tw10R21 (adiabatic wall).

the high accuracy for the velocity is retained with even a better prediction for $\tilde{U}^+$, and the prediction for $\tilde{T}$ is significantly improved. Again, this is attributed to the elevated $\mu_{t,o}$ and $y_{m\mu}$, so the logarithmic scaling in (3.6) is more strictly followed up to $y^*_{m\mu} = 210$ for this case. The TV relation is of limited help for this adiabatic case because the singular point of Pr_t, if it exists, is down to the viscous layer (see figure 6a), where κ is dominant over κ_t. Away from the singular point, Pr_t varies moderately and can be well approximated by a constant. For the heated-wall case in figure 10, the same conclusion as for figures 8 and 9 is drawn. Good agreement with DNS is realized for $\tilde{U}$ and $\tilde{T}$ in the BL-GFM-VD-TV model. The improvement for velocity is more obvious when expressed in the outer scale. The mild under-prediction in u_τ is presumably related to the relatively low Re_{δ_2} in the M2Tw19R3 and also M6Tw025R11 cases, so the outer-layer similarity of the defect velocity diminishes (see figure 5).

More attention is paid to the diabatic cases considering their ubiquity in hypersonic applications and difficulty in prediction by the baseline model. The temperature predictions for four more diabatic cases (VBL-M2Tw05R13, VBL-M5Tw19R7, ZDC-M6Tw076R17 and ZDC-M14Tw018R24) are shown in figure 11, covering the lowest and highest Ma_∞ in the dataset. In addition to the same conclusions as for figures 8–10, two more points are concluded. For the heated and moderately cooled wall cases (figure 11b,c, $T_w/T_r > 0.5$), abundant improvement in $\tilde{T}$ is achieved by BL-GFM-VD, over the BL-local model. For the highly cooled wall cases (figures 11a,d and 8c, $T_w/T_r \leq 0.5$), however, modifying only μ_t is insufficient due to the intricate variation of Pr_t near the wall. The TV relation should be further incorporated for accurate temperature prediction. As demonstrated in figure 11(e,f), the Pr_t profiles from BL-GFM-VD-TV well match the

987 A7-22
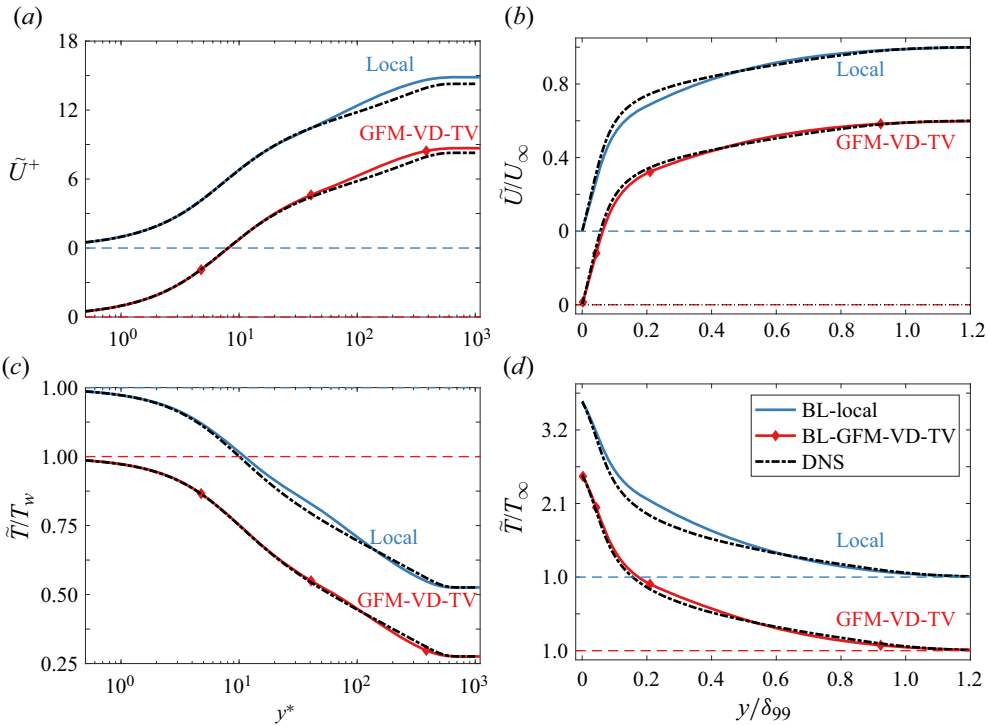
Figure 10. Same as figure 8 except for case VBL-M2Tw19R3 (heated wall).

DNS trends for these highly cooled wall cases, so the non-monotonic behaviour and the singularity of Pr_t can be reasonably modelled. For reference, the velocity predictions for the four diabatic cases are also demonstrated in figure 12. In both the inner and outer scales, the velocities by the BL-GFM-VD-TV model are in good agreement with the DNS data.

Quantitative measurements of the prediction accuracy are presented using two types of relative errors to DNS, which are defined in terms of the inner-scale logarithmic coordinate and the outer-scale normal coordinate, respectively, as

$$\epsilon_{lg,U} = \frac{\int_0^{\lg y_{up}^*} \left| \tilde{U}_{BL}^+ - \tilde{U}_{DNS}^+ \right| d \lg y^*}{\int_0^{\lg y_{up}^*} \tilde{U}_{DNS}^+ d \lg y^*}, \quad \epsilon_{n,U} = \frac{\int_0^{y_{up}} \left| \tilde{U}_{BL} - \tilde{U}_{DNS} \right| dy}{\int_0^{y_{up}} \tilde{U}_{DNS} dy}. \quad (4.1a,b)$$

The two errors for temperature, $\epsilon_{lg,T}$ and $\epsilon_{n,T}$, are defined likewise. The upper limits of the integral y_{up} for all four ϵ are fixed at $1.1\delta_{99}$. The four errors for all cases are displayed in figure 13 in the order of case numbers. Note that the algebraic averaged errors between locations are displayed for the cases with multiple streamwise locations.

As mentioned above, the BL-local model satisfactorily reproduces $\tilde{U}$ for the adiabatic cases (numbers 1–4), with $\epsilon_{lg,U} < 1.0\,\%$ and $\epsilon_{n,U} < 1.6\,\%$ for all examined. These are also the accuracy levels of the incompressible BL model. In the presence of surface heat transfer, the two ϵ_U rise a bit, and $\epsilon_{n,U}$ reaches over $3\,\%$ for the four hypersonic cases. Meanwhile, the temperature prediction has poor performance, where $\epsilon_{n,T}$ exceeds $10\,\%$ for the five hypersonic diabatic cases and even surpasses $20\,\%$ for case 12 with

987 A7-23
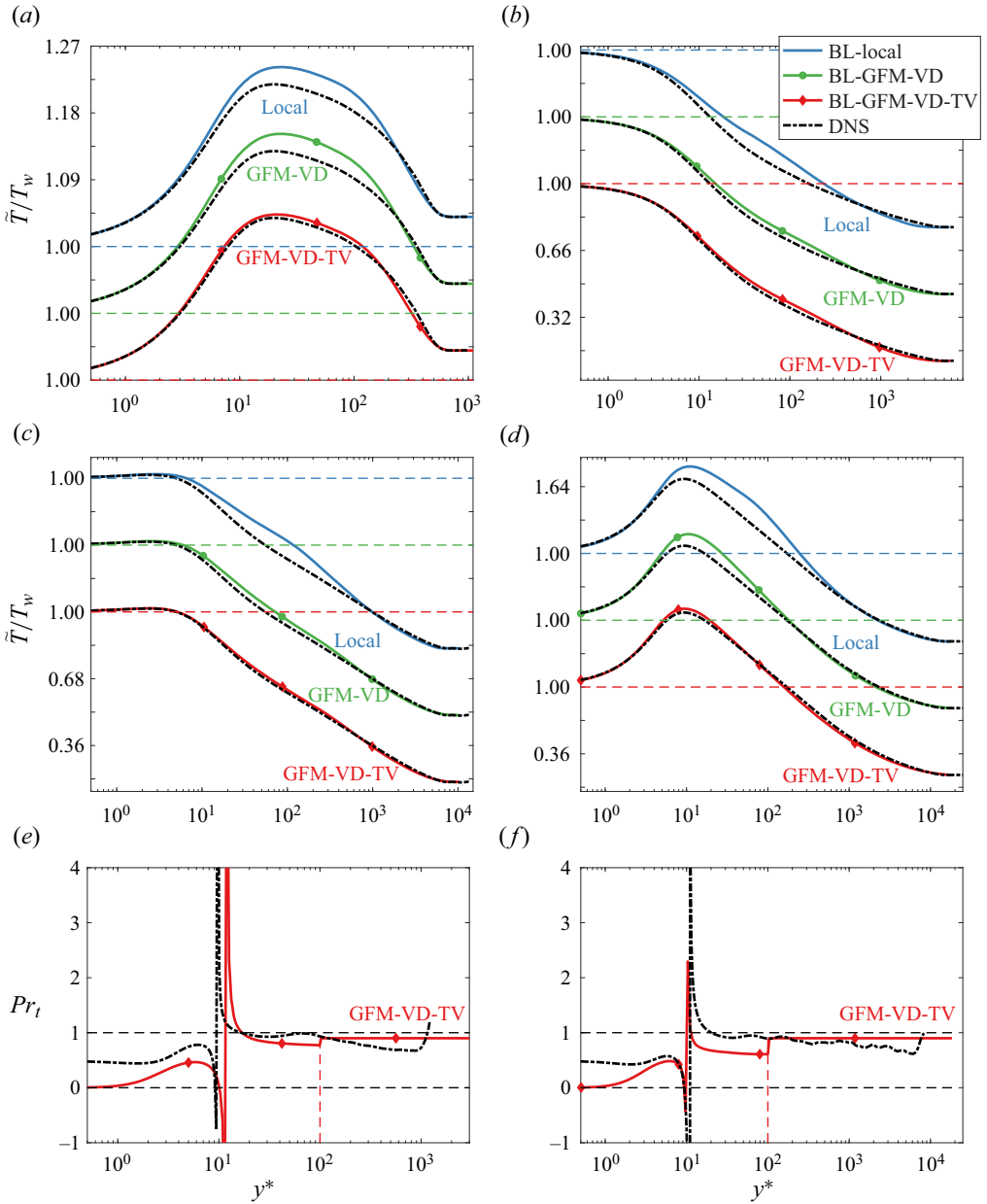
Figure 11. (*a–d*) Mean temperature and (*e–f*) turbulent Prandtl number profiles from different BL models for cases (*a*) VBL-M2Tw05R13 (cold wall), (*b*) VBL-M5Tw19R7 (heated wall), (*c*) ZDC-M6Tw076R17 (cold wall) and (*d*) ZDC-M14Tw018R24 (cold wall). Panels (*e,f*) are for the two highly cooled wall cases ZDC-M6Tw025R11 and M14Tw018R24.

a heated wall. In comparison, the velocity prediction is moderately improved using the BL-GFM-VD-TV model. The mean $\epsilon_{lg,U}$ for all cases is reduced from 1.2 % to 0.7 %, and the mean $\epsilon_{n,U}$ is from 2.5 % to 1.3 %. More importantly, the two ϵ_U from BL-GFM-VD-TV do not exhibit an obviously increasing trend with *Ma* lifted or wall-cooling strengthened, indicating enhanced model robustness by employing established relations. It is worth
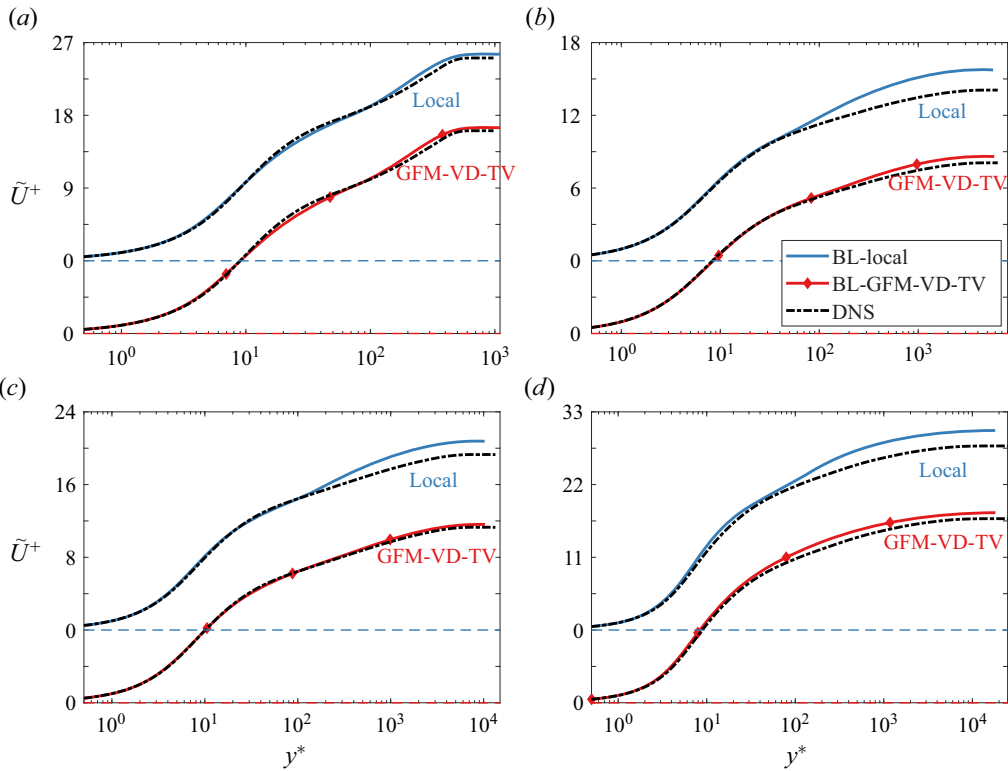
Figure 12. Same as figure 11 except for the mean streamwise velocity (four diabatic cases). (*a*) M2Tw05R13, (*b*) M5Tw19R7, (*c*) M6Tw076R17, (*d*) M14Tw018R24.

mentioning that case 7 (M6Tw025R11) is the only one where $\epsilon_{lg,U}$ is not improved, as discussed for figure 8. This is acceptable considering the imperfect collapse of the outer-layer scaling in figure 5 due to compressibility and low-*Re* effects. Compared with the velocity counterpart, a more significant improvement is realized in the temperature prediction. After deploying BL-GFM-VD-TV, $\epsilon_{lg,T}$ and $\epsilon_{n,T}$ for all cases are notably decreased. As an overall measure, the mean $\epsilon_{lg,T}$ is reduced from 1.4 % to 0.4 %, and the mean $\epsilon_{n,T}$ is reduced from 8.8 % to 3.4 %. Moreover, we plot in figure 13(*b*) the $\epsilon_{lg,T}$ from BL-GFM-VD. It is between the errors of BL-local and BL-GFM-VD-TV for each case, demonstrating that the improved temperature prediction is jointly contributed by the velocity transformations and the TV relation.

Besides the mean profiles, the wall and integral quantities are also of interest in RANS. The comparison between the BL models and DNS is listed in table 2 for the five ZDC cases at specific Re_τ, where H is the shape factor, and C_f and B_q are the non-dimensional surface friction and heat flux. First, much better predictions for integral quantities, such as H, are realized in the BL-GFM-VD-TV model, attributed to the overall improvement in mean profile shapes. Regarding the wall quantities, the BL-local model employs the TL transformation for the inner layer μ_t (see § 3.1). Since TL provides accurate scaling in the viscous layer, the wall quantities can be well predicted by the BL-local model including diabatic cases, as demonstrated by Dilley & McClinton (2001). After using BL-GFM-VD-TV, some improvements for the wall quantities can be observed, especially for u_τ and C_f. Nevertheless, not all the cases are improved at the specific limited streamwise locations, in particular the M6Tw025R11 case of relatively low Re_{δ_2}. A more
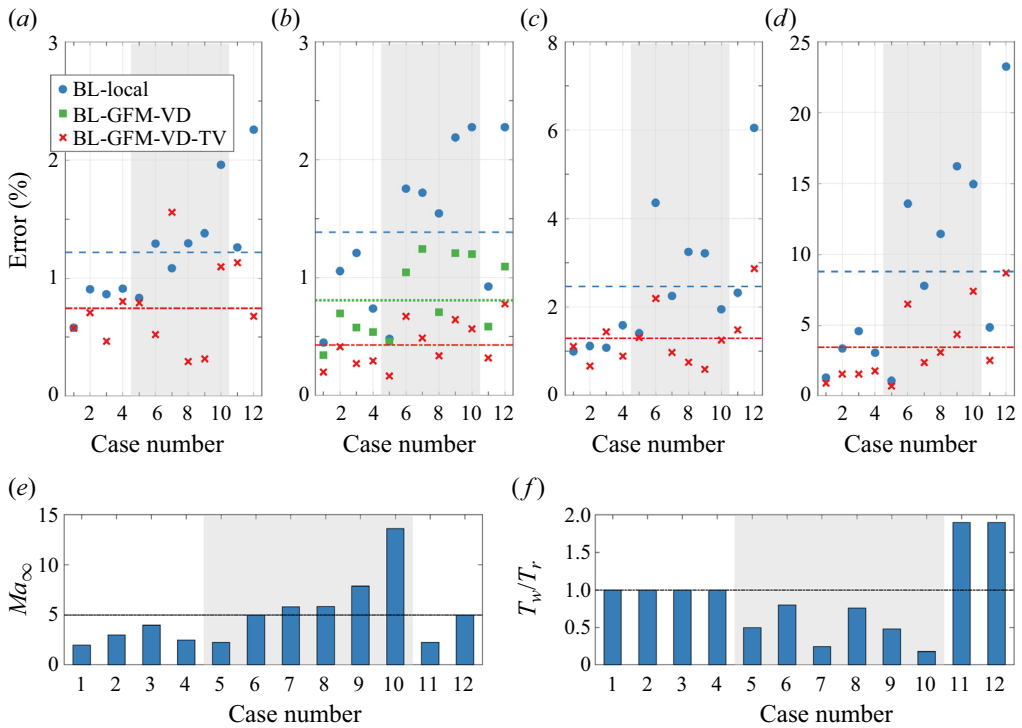
Figure 13. Relative errors of different BL models to DNS for the mean (*a,c*) streamwise velocity and (*b,d*) temperature, measured in terms of (*a,b*) logarithmic and (*c,d*) normal coordinates, respectively, where (*a*) $\epsilon_{lg,U}$, (*b*) $\epsilon_{lg,T}$, (*c*) $\epsilon_{n,U}$, (*d*) $\epsilon_{n,T}$. The horizontal lines are their average errors. For reference, the Ma_∞ and T_w/T_r in each case are plotted in panels (*e,f*). Cases 1–4 are adiabatic walls, 5–10 are cold walls and 11–12 are heated walls, as categorized in shaded areas.

comprehensive evaluation of the wall quantities is anticipated based on the data at a set of locations in each case.

5. Discussions and summary

5.1. *Discussions*

The present work is designed for ZPG boundary layers, so its applications and limitations are further discussed. First, we demonstrate a promising framework of how to incorporate well-established mean flow relations to improve the BL wall model. The module-style modification allows direct substitutions of more accurate relations in the future. Second, a highly efficient and accurate mean-flow solver is feasible using the modified BL model, which can be further combined with, for example, the resolvent analysis to obtain the fluctuation characteristics over a wide parameter space (*Ma*, *Re*, wall cooling, etc.), as done by Cossu, Pujals & Depardon (2009) for incompressible boundary layers and by Chen *et al.* (2023*a,b*) for compressible channels. Third, the two modified models can be applied to high-speed channel and pipe flows, though we anticipate that the improvement over the BL-local model will not be as large as that for the boundary layer cases. Two possible reasons are that for channel and pipe flows, the TL transformation used for the inner layer is particularly accurate, and Pr_t has no singularities in the near-wall region (e.g. Huang *et al.* 1995; Cheng & Fu 2023).

987 A7-26

Case	Solver	Re_τ	Re_θ	H	δ_v (μm)	u_τ (m s^{-1})	$-B_q$	$C_f \times 10^3$
M2p5Tw10R17	DNS	510	2835	4.1	15.0	40.6	0	2.31
	BL-local		3026	4.29	15.5	38.6	0	2.07
	GFM-VD-TV		2939	4.17	15.3	39.1	0	2.13
M6Tw025R11	DNS	450	2121	8.4	8.0	33.8	0.14	1.70
	BL-local		2181	8.96	8.4	32.2	0.132	1.55
	GFM-VD-TV		2198	8.35	8.5	31.9	0.128	1.52
M6Tw076R17	DNS	453	9455	13.6	52.6	45.1	0.02	1.00
	BL-local		10 325	14.4	55.1	41.6	0.018	0.85
	GFM-VD-TV		9492	13.7	51.6	44.4	0.019	0.97
M8Tw048R20	DNS	480	9714	17.4	73.5	54.3	0.06	0.77
	BL-local		9942	20.1	71.7	50.2	0.056	0.66
	GFM-VD-TV		9200	19.0	66.9	53.8	0.059	0.76
M14Tw018R24	DNS	646	14 408	37.6	102.4	67.6	0.19	0.40
	BL-local		13 721	43.8	109.0	62.5	0.173	0.35
	GFM-VD-TV		13 451	40.9	103.6	65.8	0.179	0.39

Table 2. Some wall and integral quantities from different BL models and DNS for the ZDC cases. The significant figures of the DNS data are the same as in the reference. Note that C_f was not listed in the reference, so it is inferred here using ρ_w and u_τ.

As discussed in § 3, the present modifications are limited to attached thin-layer flows (then $|\tilde{\omega}| = |\partial \tilde{U}_{//}/\partial n|$ or $|\partial \tilde{U}/\partial y|$), so it becomes inapplicable when other components of $\tilde{\omega}$ are non-negligible. In this sense, the modified BL model is less general than the baseline one. On the one hand, it is known that computing the attached thin-layer flow is the strength of the BL model (and other algebraic ones) over other more sophisticated turbulence models, so the present modifications to the BL model can help maximize its strength. On the other hand, further extensions to more general flows with pressure gradients, separation, etc., are under investigation and will be reported separately. Taking the pressure gradient effects as an example, model improvement is anticipated owing to the following evidence. A valuable DNS database was elaborated by Wenzel *et al.* (2019) for supersonic boundary layers (Mach 2) under both favourable and adverse pressure gradients. Their results, and also those of Bai *et al.* (2022), actively support the usage of various velocity transformations for the inner layer. With rising adverse pressure gradient strength, the VD transformation increasingly underestimates the velocity in the outer region, but it significantly reduces the compressibility effects. Moreover, Gibis *et al.* (2019) suggested appropriate compressible scalings for the outer-layer self-similarity under pressure gradients, which could, for example, improve the Rotta–Clauser parameter used in the CS model. Nevertheless, more non-ZPG DNS databases are highly desired in a range of *Ma* and wall-cooling conditions.

5.2. *Summary*

Different forms of mean-flow relations for high-speed wall-bounded turbulence, including the velocity transformation and algebraic TV relation, have been established in previous works with increasing accuracy. The combination of these relations enables an efficient and accurate recovery of the mean flow as an inverse problem, which is a solid mean to accommodate compressibility effects. This thought is utilized in this work, and the core idea is to systematically improve the BL wall model for ZPG boundary layers using various established scalings. The objective is that BL can achieve comparable accuracy

with the incompressible counterpart. Only well-established relations are adopted, and we avoid introducing any new functions or coefficients fitted by ourselves. Twelve published DNS datasets are employed for *a priori* inspiration and *a posteriori* examination. A large parameter space is covered, with Ma_∞ ranging from 2 to 14 under adiabatic, cold and heated wall conditions (T_w/T_r from 0.18 to 1.9).

The baseline BL-local model is the classical one widely used in numerous commercial solvers, which uses semilocal units in the inner-layer damping function, and assumes a prescribed Pr_t distribution. The baseline model can well reproduce the velocity for adiabatic cases, but deteriorates subject to surface heat transfer. Meanwhile, the temperature prediction has obvious deviations from DNS in both adiabatic and diabatic cases.

Three modifications are made to the formulations of μ_t and $\tilde{T}$, corresponding to the three shortcomings of the BL-local model. First, we show that the inner-layer scaling of μ_t in BL-local is equivalent to applying the TL transformation, which degrades in the logarithmic region in diabatic boundary layers. Therefore, we adopt the GFM transformation instead, for improved logarithmic scaling of μ_t. Second, the outer-layer μ_t and thus the matching location can be severely underestimated ($y_{m\mu}^*$ down to 40–60) in BL-local, so the logarithmic scaling above this low $y_{m\mu}^*$ is not followed. For improvement, we adopt the VD transformation in the outer layer based on the compressible defect velocity scaling. Third, the inner layer temperature in cold-wall cases is quite sensitive to Pr_t, and Pr_t varies considerably near the wall and exhibits a singularity around the temperature peak. Since there lacks a unified modelling of Pr_t near the wall, we design a novel two-layer formulation of $\tilde{T}$. The energy equation with constant Pr_t is only solved in the outer layer ($y > y_{mT}$), and the inner layer ($y < y_{mT}$) temperature is formulated by the algebraic quadratic TV relation. The modified model is termed BL-GFM-VD-TV, where the latter three acronyms denote the three modifications, respectively; see § 3.4.

Numerical results between all the DNS cases demonstrate that the three modifications take effect as expected. For the mean streamwise velocity, the high accuracy of the BL-local model for adiabatic cases is retained, while that for diabatic cases is improved, especially in the logarithmic region. Meanwhile, significant improvement for the temperature is realized for both adiabatic and diabatic cases, that $\tilde{T}$ is in close agreement with DNS in most cases, which has not been realized before. The mean relative errors of $\tilde{T}$ to DNS for all cases are down to 0.4 % measured in the logarithmic wall-normal coordinate and 3.4 % in the outer coordinate, only around one-third of those in the baseline model. Furthermore, *a posteriori* diagnosis suggests that the non-monotonic and singular behaviours of Pr_t in cold-wall cases can be modelled. We emphasize that modifying only μ_t is insufficient for an accurate temperature prediction in highly cooled wall cases. The TV relation should be further incorporated in the near-wall region.

Future works will be on possible extensions of the modified models to more complex configurations, and their behaviours in the flows with moderate pressure gradients.

Figure 14. Mean streamwise velocity and temperature from the standard BL model for cases (*a*) M6Tw025R11 and (*b*) M14Tw018R24. The reference data are from (*a*) Hendrickson *et al.* (2023) and (*b*) our RANS solver.

Declaration of interests. The authors report no conflict of interest.

Data availability statement. The data that support the findings of this study are available from the corresponding author upon reasonable request.

Author ORCIDs.

- Xianliang Chen https://orcid.org/0000-0002-7540-3395;
- Jianping Gan https://orcid.org/0000-0001-9827-7929;
- Lin Fu https://orcid.org/0000-0001-8979-8415.

Appendix A. Solver verification and sensitivity study

To ensure the validity of the boundary layer equations and verify our solver, we first compare the mean flow results with Hendrickson *et al.* (2023), who solved the full NS equation with BL models using the US3D code. The ZDC-M6Tw025R11 case is computed using the standard BL model. The results are shown in figure 14(*a*), and close agreement with the reference is obtained. As discussed in § 2.2, the M14Tw018R24 case is most susceptible to shock-boundary-layer interaction at the leading edge. For further validation of the boundary layer equations at such a high *Ma*, we additionally implement a second-order shock-capturing RANS simulation (Chen & Fu 2020) on a $N_x \times N_y = 300 \times 163$ mesh for this case. The comparisons of the velocity and temperature profiles are displayed in figure 14(*b*), where good agreement is demonstrated.

Next, a sensitivity study of y^*_{mT} is conducted. Three $y^*_{mT} = 50, 100, 150$ are selected, and the BL-GFM-VD-TV results for two hypersonic cases are displayed in figure 15. Basically, there is a minor difference in $\tilde{T}$ with varying y^*_{mT}. A higher y^*_{mT} tends to provide closer results to DNS near the temperature peak. On the other hand, a lower y^*_{mT} can enhance the computational robustness, especially at the first few streamwise locations. Thereby, a moderate $y^*_{mT} = 100$ is used throughout.
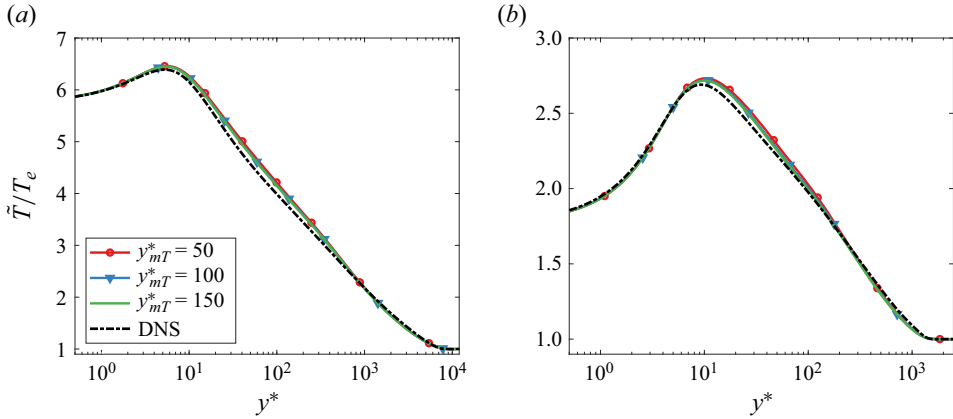
Figure 15. Mean temperature from the BL-GFM-VD-TV model with different y^*_{mT} for cases (*a*) M8Tw048R20 and (*b*) M6Tw025R11.
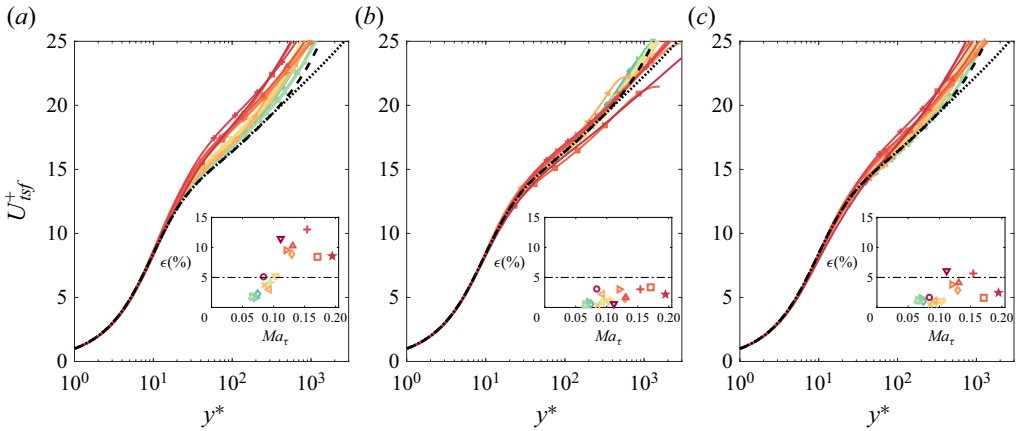
Figure 16. Transformed streamwise velocity using (*a*) TL, (*b*) GFM and (*c*) HLPP for all cases. The black dashed and dotted lines are the incompressible DNS data from Sillero, Jiménez & Moser (2013) and Lee & Moser (2015), respectively. The subpanels display the relative errors to DNS as described in Griffin *et al.* (2021) and Hasan *et al.* (2023*b*). The legends are the same as in figure 5 (pentacles represent the legends without symbols).

Appendix B. Results of the HLPP transformation

The very recent transformation of Hasan *et al.* (2023*b*) incorporates intrinsic compressibility effects by introducing a correction to the TL transformation, as

$$U^+_{HLPP}(y^*) = \int_0^{y^*} \frac{1 + \kappa_c y^* D^c}{1 + \kappa_c y^* D^i} \bar{\mu}^+ \frac{\partial y^*}{\partial y^+} \, \mathrm{d}\bar{U}^+, \quad D^c \equiv \left[1 - \exp\left(\frac{-y^*}{17 + f(Ma_\tau)} \right) \right]^2. \tag{B1a,b}$$

Here, D^i is the classical damping function as in (3.4) representing the incompressible counterpart, and D^c is the modified damping function to interpret intrinsic compressibility, where the correction function $f(Ma_\tau) = 19.3 Ma_\tau$ and Ma_τ is the friction Mach number. The transformed velocities U^+_{tsf} using TL, GFM and HLPP are shown in figure 16 for all

the DNS cases (Reynolds-averaged values), and the relative errors to DNS are displayed as a function of Ma_τ, following Hasan *et al.* (2023*b*). The mean errors (also defined based on Reynolds averages) of GFM and HLPP between all cases are approximately the same, equal to 2.2 % and 2.4 %, respectively. Note that the errors in figure 16 are somewhat differently defined from Hasan *et al.* (2023*b*) (their figure 2) because the present errors are based on the absolute value of the velocity difference, hence non-negative by definition (see equation (8) in Griffin *et al.* (2021) and (4.1*a,b*) above).

The HLPP transformation can also be employed, following the procedures in § 3.1, to improve the inner-layer scaling in the BL-local model. After incorporating VD for the outer layer and the TV relation, the final model can be termed BL-HLPP-VD-TV. We have also implemented this model and find that the mean relative errors in predicting velocity and temperature are comparable with BL-GFM-VD-TV, as expected from figure 16. Specifically, the four mean errors are $\epsilon_{lg,U} = 0.6\,\%$, $\epsilon_{lg,T} = 0.4\,\%$, $\epsilon_{n,U} = 1.3\,\%$ and $\epsilon_{n,T} = 3.5\,\%$.

REFERENCES

ABE, H. & ANTONIA, R.A. 2017 Relationship between the heat transfer law and the scalar dissipation function in a turbulent channel flow. *J. Fluid Mech.* **830**, 300–325.

BAI, T., CHENG, C., GRIFFIN, K.P., LI, X. & FU, L. 2023 Study of the vortex structure in compressible wall-bounded turbulence. *Phys. Rev. Fluids* **8** (12), 124603.

BAI, T., GRIFFIN, K.P. & FU, L. 2022 Compressible velocity transformations for various noncanonical wall-bounded turbulent flows. *AIAA J.* **60** (7), 4325–4337.

BALDWIN, B. & LOMAX, H. 1978 Thin-layer approximation and algebraic model for separated turbulent flows. In *16th Aerospace Sciences Meeting*. AIAA.

BLOTTNER, F.G. 1963 Chemical nonequilibrium boundary layer. *J. Spacecr. Rockets* **2** (2), 232–240.

BRADSHAW, P. 1977 Compressible turbulent shear layers. *Annu. Rev. Fluid Mech.* **9** (1), 33–52.

CANDLER, G.V., JOHNSON, H.B., NOMPELIS, I., GIDZAK, V.M., SUBBAREDDY, P.K. & BARNHARDT, M. 2015 Development of the US3D code for advanced compressible and reacting flow simulations. In *53rd AIAA Aerospace Sciences Meeting*. AIAA.

CATRIS, S. & AUPOIX, B. 2000 Density corrections for turbulence models. *Aerosp. Sci. Technol.* **4** (1), 1–11.

CEBECI, T. & SMITH, A.M.O. 1974 *Analysis of Turbulent Boundary Layers*. Academic Press, Elsevier.

CHEATWOOD, F.M. & THOMPSON, R.A. 1993 The addition of algebraic turbulence modeling to program LAURA. *Tech. Rep.* TM-107758. NASA Langley Research Center.

CHEN, X., CHENG, C., FU, L. & GAN, J. 2023*a* Linear response analysis of supersonic turbulent channel flows with a large parameter space. *J. Fluid Mech.* **962**, A7.

CHEN, X., CHENG, C., GAN, J. & FU, L. 2023*b* Study of the linear models in estimating coherent velocity and temperature structures for compressible turbulent channel flows. *J. Fluid Mech.* **973**, A36.

CHEN, X. & FU, S. 2020 Convergence acceleration for high-order shock-fitting methods in hypersonic flow applications with efficient implicit time-stepping schemes. *Comput. Fluids* **210**, 104668.

CHEN, X., WANG, L. & FU, S. 2021 Parabolized stability analysis of hypersonic thermal-chemical nonequilibrium boundary-layer flows. *AIAA J.* **59** (7), 2382–2395.

CHEN, X., WANG, L. & FU, S. 2022*a* Energy transfer of hypersonic and high-enthalpy boundary layer instabilities and transition. *Phys. Rev. Fluids* **7** (3), 033901.

CHEN, X., XI, Y., REN, J. & FU, S. 2022*b* Cross-flow vortices and their secondary instabilities in hypersonic and high-enthalpy boundary layers. *J. Fluid Mech.* **947**, A25.

CHENG, C., CHEN, X., ZHU, W., SHYY, W. & FU, L. 2024 Progress in physical modeling of compressible wall-bounded turbulent flows. *Acta Mech. Sin.* **40**, 323663.

CHENG, C. & FU, L. 2022 Large-scale motions and self-similar structures in compressible turbulent channel flows. *Phys. Rev. Fluids* **7** (11), 114604.

CHENG, C. & FU, L. 2023 Linear-model-based study of the coupling between velocity and temperature fields in compressible turbulent channel flows. *J. Fluid Mech.* **964**, A15.

CLAUSER, F.H. 1956 The turbulent boundary layer. *Adv. Appl. Mech.* **4**, 1–51.

COGO, M., SALVADORE, F., PICANO, F. & BERNARDINI, M. 2022 Direct numerical simulation of supersonic and hypersonic turbulent boundary layers at moderate-high Reynolds numbers and isothermal wall condition. *J. Fluid Mech.* **945**, A30.

COLEMAN, G.N., KIM, J. & MOSER, R.D. 1995 A numerical study of turbulent supersonic isothermal-wall channel flow. *J. Fluid Mech.* **305**, 159–183.

COLES, D. 1956 The law of the wake in the turbulent boundary layer. *J. Fluid Mech.* **1** (2), 191–226.

COSSU, C., PUJALS, G. & DEPARDON, S. 2009 Optimal transient growth and very large-scale structures in turbulent boundary layers. *J. Fluid Mech.* **619**, 79–94.

DEGANI, D. & SCHIFF, L. 1983 Computation of supersonic viscous flows around pointed bodies at large incidence. In *21st Aerospace Sciences Meeting*. AIAA.

DILLEY, A.D. & MCCLINTON, C.R. 2001 Evaluation of CFD turbulent heating prediction techniques and comparison with hypersonic experimental data. *Tech. Rep.* CR-2001-210837. NASA Langley Research Center.

VAN DRIEST, E.R. 1951 Turbulent boundary layer in compressible fluids. *J. Aeronaut. Sci.* **18** (3), 145–160.

VAN DRIEST, E.R. 1956 On turbulent flow near a wall. *J. Aeronaut. Sci.* **23** (11), 1007–1011.

DUAN, L., BEEKMAN, I. & MARTÍN, M.P. 2010 Direct numerical simulation of hypersonic turbulent boundary layers. Part 2. Effect of wall temperature. *J. Fluid Mech.* **655**, 419–445.

DUAN, L., BEEKMAN, I. & MARTÍN, M.P. 2011 Direct numerical simulation of hypersonic turbulent boundary layers. Part 3. Effect of Mach number. *J. Fluid Mech.* **672**, 245–267.

DUAN, L. & MARTÍN, M.P. 2011 Direct numerical simulation of hypersonic turbulent boundary layers. Part 4. Effect of high enthalpy. *J. Fluid Mech.* **684**, 25–59.

FERNHOLZ, H.-H. & FINLEY, P.J. 1980 A critical commentary on mean flow data for two-dimensional compressible turbulent boundary layers. *Tech. Rep.* AGARD-AG-253. NATO.

FU, L., BOSE, S. & MOIN, P. 2022 Prediction of aerothermal characteristics of a generic hypersonic inlet flow. *Theor. Comput. Fluid Dyn.* **36** (2), 345–368.

FU, L., KARP, M., BOSE, S.T., MOIN, P. & URZAY, J. 2021 Shock-induced heating and transition to turbulence in a hypersonic boundary layer. *J. Fluid Mech.* **909**, A8.

GATSKI, T.B. & BONNET, J.-P. 2013 *Compressibility, Turbulence and High Speed Flow*, 2nd edn. Academic Press.

GIBIS, T., WENZEL, C., KLOKER, M. & RIST, U. 2019 Self-similar compressible turbulent boundary layers with pressure gradients. Part 2. Self-similarity analysis of the outer layer. *J. Fluid Mech.* **880**, 284–325.

GRIFFIN, K.P., FU, L. & MOIN, P. 2021 Velocity transformation for compressible wall-bounded turbulent flows with and without heat transfer. *Proc. Natl Acad. Sci. USA* **118** (34), e2111144118.

GRIFFIN, K.P., FU, L. & MOIN, P. 2023 Near-wall model for compressible turbulent boundary layers based on an inverse velocity transformation. *J. Fluid Mech.* **970**, A36.

GUARINI, S.E., MOSER, R.D., SHARIFF, K. & WRAY, A. 2000 Direct numerical simulation of a supersonic turbulent boundary layer at Mach 2.5. *J. Fluid Mech.* **414**, 1–33.

GUPTA, R.N., LEE, K.P., ZOBY, E.V., MOSS, J.N. & THOMPSON, R.A. 1990 Hypersonic viscous shock-layer solutions over long slender bodies. I. High Reynolds number flows. *J. Spacecr. Rockets* **27** (2), 175–184.

HASAN, A.M., LARSSON, J., PIROZZOLI, S. & PECNIK, R. 2023*a* Estimating mean profiles and fluxes in high-speed turbulent boundary layers using inner/outer-layer scalings. *AIAA J.* **62** (2), 848–853.

HASAN, A.M., LARSSON, J., PIROZZOLI, S. & PECNIK, R. 2023*b* Incorporating intrinsic compressibility effects in velocity transformations for wall-bounded turbulent flows. *Phys. Rev. Fluids* **8** (11), L112601.

HENDRICKSON, T.R., SUBBAREDDY, P. & CANDLER, G.V. 2022 Improving eddy viscosity based turbulence models for high speed, cold wall flows. In *AIAA SCITECH 2022 Forum*. AIAA.

HENDRICKSON, T.R., SUBBAREDDY, P., CANDLER, G.V. & MACDONALD, R.L. 2023 Applying compressible transformations to wall modeled LES of cold wall flat plate boundary layers. In *AIAA SCITECH 2023 Forum*. AIAA.

HIRAI, R., PECNIK, R. & KAWAI, S. 2021 Effects of the semi-local Reynolds number in scaling turbulent statistics for wall heated/cooled supersonic turbulent boundary layers. *Phys. Rev. Fluids* **6** (12), 124603.

HUANG, P.G., BRADSHAW, P. & COAKLEY, T.J. 1993 Skin friction and velocity profile family for compressible turbulent boundary layers. *AIAA J.* **31** (9), 1600–1604.

HUANG, P.G., COLEMAN, G.N. & BRADSHAW, P. 1995 Compressible turbulent channel flows: DNS results and modelling. *J. Fluid Mech.* **305**, 185–218.

HUANG, P.G., COLEMAN, G.N., SPALART, P.R. & YANG, X.I.A. 2023 Velocity and temperature scalings leading to compressible laws of the wall. *J. Fluid Mech.* **977**, A49.

HUANG, J., DUAN, L. & CHOUDHARI, M.M. 2022 Direct numerical simulation of hypersonic turbulent boundary layers: effect of spatial evolution and Reynolds number. *J. Fluid Mech.* **937**, A3.

JOHNSON, D.A. & KING, L.S. 1985 A mathematically simple turbulence closure model for attached and separated turbulent boundary layers. *AIAA J.* **23** (11), 1684–1692.

KAMOGAWA, R., TAMAKI, Y. & KAWAI, S. 2023 Ordinary-differential-equation-based nonequilibrium wall modeling for large-eddy simulation. *Phys. Rev. Fluids* **8** (6), 064605.

KLEBANOFF, P.S. 1955 Characteristics of turbulence in boundary layer with zero pressure gradient. *Tech. Rep.* NACA Report 1247. NACA.

KUMAR, V. & LARSSON, J. 2022 Modular method for estimation of velocity and temperature profiles in high-speed boundary layers. *AIAA J.* **60** (9), 5165–5172.

LAGHA, M., KIM, J., ELDREDGE, J.D. & ZHONG, X. 2011 A numerical study of compressible turbulent boundary layers. *Phys. Fluids* **23** (1), 015106.

LEE, M. & MOSER, R.D. 2015 Direct numerical simulation of turbulent channel flow up to $Re_\tau = 5200$. *J. Fluid Mech.* **774**, 395–415.

LUSHER, D.J. & COLEMAN, G.N. 2022 Numerical study of the turbulent Prandtl number in supersonic plane-channel flow – the effect of thermal boundary conditions. *Tech. Rep.* TM-20220010483. NASA Langley Research Center.

MAISE, G. & MCDONALD, H. 1968 Mixing length and kinematic eddy viscosity in a compressible boundary layer. *AIAA J.* **6** (1), 73–80.

MO, F. & GAO, Z. 2024 A new wall function method for hypersonic laminar boundary layers. *J. Fluid Mech.* **981**, A9.

MODESTI, D. & PIROZZOLI, S. 2019 Direct numerical simulation of supersonic pipe flow at moderate Reynolds number. *Intl J. Heat Fluid Flow* **76**, 100–112.

MONKEWITZ, P.A., CHAUHAN, K.A. & NAGIB, H.M. 2007 Self-consistent high-Reynolds-number asymptotics for zero-pressure-gradient turbulent boundary layers. *Phys. Fluids* **19** (11), 115101.

MORKOVIN, M.V. 1962 Effects of compressibility on turbulent flows. In *The Mechanics of Turbulence* (ed. A. Favre), pp. 367–380. AIAA.

NAGIB, H.M., CHAUHAN, K.A. & MONKEWITZ, P.A. 2007 Approach to an asymptotic state for zero pressure gradient turbulent boundary layers. *Phil. Trans. R. Soc. Lond.* A **365** (1852), 755–770.

OTERO RODRIGUEZ, G.J., PATEL, A., DIEZ SANHUEZA, R. & PECNIK, R. 2018 Turbulence modelling for flows with strong variations in thermo-physical properties. *Intl J. Heat Fluid Flow* **73**, 114–123.

PANARAS, A.G. 1997 Algebraic turbulence modeling for swept shock-wave/turbulent boundary-layer interactions. *AIAA J.* **35** (3), 456–463.

PASSIATORE, D., SCIACOVELLI, L., CINNELLA, P. & PASCAZIO, G. 2022 Thermochemical non-equilibrium effects in turbulent hypersonic boundary layers. *J. Fluid Mech.* **941**, A21.

PIROZZOLI, S. & BERNARDINI, M. 2011 Turbulence in supersonic boundary layers at moderate Reynolds number. *J. Fluid Mech.* **688**, 120–168.

PIROZZOLI, S. & BERNARDINI, M. 2013 Probing high-Reynolds-number effects in numerical boundary layers. *Phys. Fluids* **25** (2), 021704.

PIROZZOLI, S., GRASSO, F. & GATSKI, T.B. 2004 Direct numerical simulation and analysis of a spatially evolving supersonic turbulent boundary layer at $M = 2.25$. *Phys. Fluids* **16** (3), 530–545.

PROBSTEIN, R.F. & ELLIOTT, D. 1956 The transverse curvature effect in compressible axially symmetric laminar boundary-layer flow. *J. Aeronaut. Sci.* **23** (3), 208–224.

RUMSEY, C.L., BIEDRON, R.T. & THOMAS, J.L. 1997 CFL3D: its history and some recent applications. *Tech. Rep.* TM-112861. NASA Langley Research Center.

SCHLATTER, P. & ÖRLÜ, R. 2010 Assessment of direct numerical simulation data of turbulent boundary layers. *J. Fluid Mech.* **659**, 116–126.

SHANG, J.S., HANKEY, W.L. & DWOYER, D.L. 1973 Numerical analysis of eddy viscosity models in supersonic turbulent boundary layers. *AIAA J.* **11** (12), 1677–1683.

SILLERO, J.A., JIMÉNEZ, J. & MOSER, R.D. 2013 One-point statistics for turbulent wall-bounded flows at Reynolds numbers up to $\delta^+ \approx 2000$. *Phys. Fluids* **25** (10), 105102.

SMITS, A.J. & DUSSAUGE, J.-P. 2006 *Turbulent Shear Layers in Supersonic Flow*, 2nd edn. Springer Science & Business Media.

SONG, Y., ZHANG, P. & XIA, Z. 2023 Predicting mean profiles in compressible turbulent channel and pipe flows. *Phys. Rev. Fluids* **8** (3), 034604.

SRINIVASAN, S., BITTNER, R. & BOBSKILL, G. 1993 Summary of the GASP code application and evaluation effort for scramjet combustor flowfields. In *29th Joint Propulsion Conference and Exhibit*. AIAA.

SUBBAREDDY, P. & CANDLER, G. 2012 DNS of transition to turbulence in a Mach 6 boundary layer. In *43rd AIAA Thermophysics Conference*. AIAA.

TOWNEND, L.H., MUYLAERT, J., WALPOT, L. & VENNEMANN, D. 1999 A review of European code-validation studies in high-enthalpy flow. *Phil. Trans. R. Soc. Lond.* A **357** (1759), 2249–2278.

TRETTEL, A. & LARSSON, J. 2016 Mean velocity scaling for compressible wall turbulence with heat transfer. *Phys. Fluids* **28** (2), 026102.

VOLPIANI, P.S., BERNARDINI, M. & LARSSON, J. 2018 Effects of a nonadiabatic wall on supersonic shock/boundary-layer interactions. *Phys. Rev. Fluids* **3** (8), 083401.

VOLPIANI, P.S., BERNARDINI, M. & LARSSON, J. 2020 Effects of a nonadiabatic wall on hypersonic shock/boundary-layer interactions. *Phys. Rev. Fluids* **5** (1), 014602.

WALZ, A. 1969 *Boundary Layers of Flow and Temperature*. MIT Press.

WENZEL, C., GIBIS, T., KLOKER, M. & RIST, U. 2019 Self-similar compressible turbulent boundary layers with pressure gradients. Part 1. Direct numerical simulation and assessment of Morkovin's hypothesis. *J. Fluid Mech.* **880**, 239–283.

WENZEL, C., SELENT, B., KLOKER, M. & RIST, U. 2018 DNS of compressible turbulent boundary layers and assessment of data/scaling-law quality. *J. Fluid Mech.* **842**, 428–468.

WHITE, F.M. 2006 *Viscous Fluid Flow*, 3rd edn. McGraw Hill.

WILCOX, D.C. 2006 *Turbulence modeling for CFD*, 3rd edn. DCW Industries.

YANG, X.I.A. & LV, Y. 2018 A semi-locally scaled eddy viscosity formulation for LES wall models and flows at high speeds. *Theor. Comput. Fluid Dyn.* **32** (5), 617–627.

YORK, B. & KNIGHT, D. 1985 Calculation of two-dimensional turbulent boundary layers using the Baldwin–Lomax model. *AIAA J.* **23** (12), 1849–1850.

ZHANG, Y.-S., BI, W.-T., HUSSAIN, F., LI, X.-L. & SHE, Z.-S. 2012 Mach-number-invariant mean-velocity profile of compressible turbulent boundary layers. *Phys. Rev. Lett.* **109** (5), 054502.

ZHANG, Y.-S., BI, W.-T., HUSSAIN, F. & SHE, Z.-S. 2014 A generalized Reynolds analogy for compressible wall-bounded turbulent flows. *J. Fluid Mech.* **739**, 392–420.

ZHANG, C., DUAN, L. & CHOUDHARI, M.M. 2018 Direct numerical simulation database for supersonic and hypersonic turbulent boundary layers. *AIAA J.* **56** (11), 4297–4311.

ZHANG, P.-J.-Y., WAN, Z.-H., LIU, N.-S., SUN, D.-J. & LU, X.-Y. 2022 Wall-cooling effects on pressure fluctuations in compressible turbulent boundary layers from subsonic to hypersonic regimes. *J. Fluid Mech.* **946**, A14.